Uncertainty evaluation of the caesium fountain clock PTB-CSF2

V. Gerginov, N. Nemitz, S. Weyers, R. Schröder, D. Griebsch and R. Wynands

Physikalisch-Technische Bundesanstalt (PTB)
Bundesallee 100, 38116 Braunschweig, Germany

E-mail: vladislav.gerginov@ptb.de

Abstract.

The uncertainty evaluation of CSF2, the second caesium fountain primary frequency standard at PTB, is presented. The fountain uses optical molasses to cool atoms down to 0.6 μK. The atoms are launched vertically in a moving optical molasses, and state-selected in the $|F = 3, m_F = 0\rangle$ hyperfine ground state. During their ballistic flight, the atoms interact twice with a microwave field, thus completing the Ramsey interaction. With a launch height of 36.5 cm above the cavity center, the central Ramsey fringe has a width of 0.9 Hz. About 3×10^4 atoms, 30% of the initial number in the $|F = 3, m_F = 0\rangle$ state, are detected after their second interaction with the microwave field. Stabilizing the microwave frequency to the center of the central Ramsey fringe, a typical relative frequency instability of $2.5 \times 10^{-13}\,(\tau/\mathrm{s})^{-1/2}$ is obtained. The CSF2 systematic uncertainty for realizing the SI second is estimated as 0.80×10^{-15}. First comparisons with the fountain CSF1 at the Physikalisch-Technische Bundesanstalt and other fountain frequency standards worldwide demonstrate agreement within the stated uncertainties.

1. Introduction

The transition frequency between the unperturbed ground state hyperfine components of neutral ^{133}Cs (caesium) is presently used in the definition of the second in the International System of Units (SI). The definition of the second is realized in practice by primary caesium atomic frequency standards (clocks). Presently, the most accurate caesium clocks are based on the fountain geometry [1]. During the last decade, several caesium fountain clocks serving as primary frequency standards have been developed worldwide [2, 3, 4, 5, 6, 7, 8, 9]. The technique used in these clocks leads to a superior performance compared to conventional caesium beam clocks, because of longer interaction times and reduced systematic uncertainties. For this reason, these standards have become more and more important for the calibration of International Atomic Time (TAI). Nowadays relative uncertainties well below the 10^{-15} level [2, 5, 6] and instabilities in the low $10^{-14}(\tau/\mathrm{s})^{-1/2}$ range [2] are obtained. Recent developments demonstrated new ways to reach the quantum limit of their instabilities [2, 10, 11] and to better control shifts due to cold collisions [12, 13]. There is also significant progress towards the implementation of cryogenic fountains with reduced uncertainty contribution due to the blackbody radiation shift [14, 15].

Following the development and operation of the first caesium fountain CSF1 [3, 4] at the Physikalisch-Technische Bundesanstalt (PTB), a new primary frequency standard, the caesium fountain CSF2, was constructed and put into operation. The goal was to implement several improvements compared to CSF1 in order to reach a lower systematic uncertainty [16]. At the same time the availability of two fountain clocks enables better evaluations of each standard using the other standard as a stable reference. In 2006 CSF2 became operational for the first time [16]. During 2006 - 2008 several technical improvements were implemented, which include state-selection, improved Ramsey fringe contrast, and lower atomic cloud temperature. Since December 2008, the frequency uncertainty of the clock has been evaluated, and several comparisons with CSF1 were performed.

2. Design of CSF2 and its optical setup

2.1. Setup of the fountain

In the fountain structure shown in Figure 1 a cold sample of caesium atoms is launched vertically. At the top of the drift tube, an ion getter pump is attached, which evacuates the drift tube. The pressure at the top ion pump is 5×10^{-8} Pa. Another ion getter pump reduces the residual gas pressure at the bottom of the structure to 8×10^{-6} Pa. A pinch-off tube reservoir holds an ampule of caesium at room temperature, providing caesium vapor. The atoms are cooled in an optical molasses using polarization gradient cooling. The utilization of the $(1,1,1)$ geometry for the cooling lasers allows for large diameters of the laser beams used for the optical molasses. Each of the six molasses laser beams (diameter 22 mm, $e^{-1/2}$ level) is delivered by its own polarization-maintaining optical

fiber and expanded by a collimator mounted directly on the fountain structure. Each pair of counter-propagating laser beams has orthogonal linear polarizations, determined by polarizers mounted inside the output couplers. The output couplers were aligned with respect to output beam direction and collimation before attaching them to the vacuum flanges. The flanges have been manufactured with nominal directional accuracy of better than 1 mrad. The entire cooling zone (including the laser beam collimators) can be pivoted around its center on a ball-joint, allowing a fine tuning of the launch direction. Thus a sub-milliradian alignment of the launch direction could be performed, by which the number of returned atoms was increased by a factor of 3 over that detected with pre-aligned launch direction.

A state-selection microwave cavity is mounted 18.5 cm above the cooling zone. The residual thermal caesium vapor pressure above this cavity is reduced by graphite getters which extend between the state-selection cavity and the detection zones along the vacuum vessel walls. Two detection zones located 30 cm above the cooling zone are vertically separated by 2.3 cm. The two zones are used to detect separately the atoms in the $|F = 4\rangle$ (upper zone) and the $|F = 3\rangle$ (lower zone) states, where F is the total angular momentum quantum number of the specific atomic state. The main (Ramsey) microwave cavity is located 63.5 cm above the cooling zone. The atoms are typically launched to 36.5 cm above the Ramsey cavity, resulting in a Ramsey interaction time T_R of 0.54 s. The diameter of the drift tube above the Ramsey cavity is tapered from 140 mm to 50 mm diameter to reduce the interior wall outgassing and to decrease the pumped volume. The drift tube is made of copper to ensure good temperature uniformity along the atomic trajectory. PT100 temperature sensors are glued to the external wall of the copper drift tube at four positions along its length.

The magnetic fields created by the ion getter pumps at the top and at the bottom of CSF2 are shielded in order to improve the magnetic field homogeneity along the atomic trajectory. The static background magnetic field in the cooling zone is compensated by three sets of large $(60 \times 60)\,\mathrm{cm}^2$ square coil pairs. Three cylindrical magnetic shields enclose the drift tube and the Ramsey cavity, as shown in Figure 1. The bottom of the outer shield is 40 cm above the cooling zone. Inside the shields, a homogeneous magnetic field (C-field) is created by a precision-wound coil. Close to each end of the main coil, two co-axial short-length coils with the same diameter as the main coil are added to improve the axial homogeneity of the field in the end regions. Additional short co-axial coils with small diameters are positioned close to the lower and upper opening of the shields and enable a further fine-tuning of the magnetic field along the atomic trajectory.

2.2. Optical system

For the optical setup single-mode diode lasers operating in the vicinity of the caesium D_2 transition (852 nm) are used. The optical system consists of a 45 mW master laser (external-cavity diode laser with <1 MHz linewidth), two 150 mW slave lasers injection-

locked by the master, and a 100 mW repumping laser (external-cavity diode laser with <1 MHz linewidth). The optical setup is shown in Figure 2.

A portion of the master laser output is split from the main laser beam and sent through an acousto-optic modulator AOM_1. This shifts the optical frequency of the laser beam to the red by 126 MHz. The red-detuned laser beam is then sent to a saturated absorption spectroscopy setup (SA-M) which uses a caesium vapor cell kept at room temperature. The $|F = 4\rangle \rightarrow |F' = 4, 5\rangle$ saturated absorption crossover optical resonance is used for frequency locking the frequency-detuned laser beam. For this purpose the frequency of AOM_1 is square-wave modulated at 50 kHz with 2.5 MHz depth to implement a phase-sensitive detection for the laser lock. The rest of the unmodulated master laser output light (with frequency close to the $|F = 4\rangle \rightarrow |F' = 5\rangle$ atomic transition frequency) is sent through another acousto-optic modulator AOM_2 in a double-pass configuration, and then to the two slave lasers for injection locking. AOM_2 performs (together with AOM_3 – AOM_5) the proper frequency detuning during the cooling and detection stages and is used for the frequency ramp during the postcooling stage of the molasses. The light of the first (second) slave laser is sent through a double-pass acousto-optic modulator AOM_3 (AOM_4) and then to the three polarization-maintaining optical fibers providing the laser beams for cooling from above (below). The laser power in each molasses laser beam is ~ 5 mW. The acousto-optic modulators AOM_3 and AOM_4 also provide the frequency detuning required to create a moving optical molasses for launching the atoms. Finally, they provide the laser intensity ramp used during the postcooling stage of the molasses.

To implement the locking of the repumping laser, the laser frequency is modulated at 50 kHz using a sinusoidal current modulation. A small part of the repumping laser light is sent to a saturated absorption setup (SA-R) and is used for locking the laser frequency to the $|F = 3\rangle \rightarrow |F' = 3, 4\rangle$ saturated absorption crossover optical resonance. The rest of the repumping laser light is sent through an acousto-optic modulator AOM_6 which shifts the laser frequency into resonance with the $|F = 3\rangle \rightarrow |F' = 4\rangle$ atomic transition. The major part of the light which passes through AOM_6 is combined with the output light of the second slave laser, and is sent to the molasses region via the three polarization-maintaining optical fibers providing the laser beams for cooling from below. The total power of the repumping laser light in the molasses region is 7.5 mW. The minor part of the repumping laser light is sent to the lower detection zone using a polarization-maintaining fiber.

Part of the output light of the first slave laser, after passing through the acousto-optic modulator AOM_5, has its frequency tuned to the vicinity of the $|F = 4\rangle \rightarrow |F' = 5\rangle$ transition in order to maximize the number of fluorescence photons per atom [17]. The light is sent via a polarization-maintaining optical fiber to the detection zones. Using a single fiber for the light for both detection zones results in common-mode noise (polarization and amplitude variations of the light at the fiber output) in the two detection zones, which is largely suppressed using a normalization procedure described below. Behind the fiber output coupler a collimated laser beam of 22 mm diameter

($e^{-1/2}$ level) is obtained and sent to both detection zones. Two rectangular apertures (height 0.8 cm, width 1 cm) are used to define the cross-section of the laser beams in each detection zone. The polarization of the light in the detection zones is circular.

The detection laser light passes through the vacuum system and is retro-reflected by a mirror to form a standing wave in both detection zones. The retro-reflecting mirror is blocked at the bottom part of the upper detection zone to locally create a running light wave in order to push away the atoms in the state $|F = 4\rangle$ after their detection in the top part of the upper detection zone. For detecting the atoms in state $|F = 3\rangle$ repumping laser light is sent to the lower detection zone via a separate polarization-maintaining optical fiber. Thus the $|F = 3\rangle$-atoms are pumped into the $|F = 4\rangle$ state and exposed to the laser light tuned to the vicinity of the cycling transition $|F = 4\rangle \rightarrow |F' = 5\rangle$ in order to be effectively detected.

The scattered light from the atoms in the states $|F = 4\rangle$ and $|F = 3\rangle$ is collected separately by two identical optical systems in the two opposite directions orthogonal to the laser beams and the atomic trajectory. The positions of the respective optical axes of the optical systems are equal to the heights of the upper and lower detection laser beams, respectively. The optical systems image the respective fluorescence volumes on large-area (1 cm^2) photodiodes, resulting in photon detection efficiencies of several percent. Due to the high number of scattered photons ($\sim 10^4$) per atom it is thus ensured that the atom detection efficiency is close to 100% in both detection zones.

2.3. Ramsey microwave cavity and state-selection cavity

The TE_{011} Ramsey cavity is identical to the Ramsey cavity used in CSF1 and has been described in detail previously [18, 19, 3]. It was designed to have low transversal phase variations across the cavity openings of 1 cm diameter. The cavity made from OFHC copper is cylindrical, with inner dimensions of 48.4 mm diameter and 28.5 mm height. The coaxial line that carries the microwave signal is tightly coupled with a bent waveguide, in which a standing wave forms. The microwave TE_{011} mode is fed from the bent waveguide by two symmetric slits (10.8 mm length and 2 mm width) at diametrically opposite positions of the cavity. The tight coupling of the cavity results in a relatively low loaded intrinsic quality factor $Q \approx 2000$, which reduces the effect of cavity resonance detuning (for instance by thermal effects) on the microwave field amplitude, compared to the case of weak coupling. Therefore, the quality of the temperature stabilization by the air conditioning of the clock hall (± 0.2 K), where CSF2 is located, is sufficient to provide proper performance, so that no extra temperature stabilization of the cavity itself is required. In order to avoid microwave leakage from the cavity, two cutoff tubes of 10 mm inner diameter and 70 mm length are attached to the lower and upper ends of the cavity, centered on the cavity axis.

A rectangular TE_{201} state-selection cavity made from stainless steel is located between the cooling and the detection region. It is used to transfer the atoms from the $|4, 0\rangle$ state to the $|3, 0\rangle$ state. The horizontal detection laser beams are used to push

away atoms that remained in the state $|F = 4\rangle$ after the state-selection process.

2.4. Frequency synthesis

The frequency synthesis of CSF2 is identical to the one used for the evaluation of CSF1 [20, 3]. The microwave field at 9192 MHz is synthesized from a low-noise BVA voltage-controlled quartz oscillator (DEQTRON, OSA 8607-BM, osc.#351). The 5 MHz output of the quartz oscillator is multiplied to 9200 MHz and mixed with the signal of a dielectric resonator oscillator (DRO) at a frequency of 9192.6 MHz whose output signal is used for interrogation of the atomic transition. The beat signal at 7.36 MHz between the DRO frequency and the 9.2 GHz (derived from the quartz signal) is mixed with a 7.36 MHz signal from a frequency synthesizer referenced to the 5 MHz output of the crystal oscillator. The mixer output is used to implement a phase lock of the DRO. In clock operation mode, the output of the frequency synthesizer is square-wave modulated in phase with subsequent fountain cycles. The modulation depth is typically half of the Ramsey fringe width of 0.9 Hz.

The computer controlling the operation of the fountain compares the transition probabilities for the two frequency values of the square-wave modulation to derive a frequency error signal. It implements a digital integrator and generates a control voltage using a data acquisition board. The control voltage is applied to an analog PI controller and then to the control voltage input of the quartz oscillator (time constant: 17 s). The parameters of the servo were chosen such that the digital integrator handles the rapid fluctuations of the crystal oscillator frequency, while the analog circuit handles the necessary DC part and long-term variation of the applied quartz control-voltage required by quartz oscillator frequency changes due to aging.

2.5. Fountain cycle

The typical fountain cycle is described in [1] and is only briefly discussed here for standard operation of CSF2. The atoms are loaded in an optical molasses configuration, typically for 500 ms. During the loading, the optical frequency of the molasses laser beams is detuned by ~ 11 MHz below the cycling $|F = 4\rangle \rightarrow |F' = 5\rangle$ transition. At the end of the loading period, the molasses and repumping light is extinguished, and the atoms are allowed to drop due to gravity for 10 ms to allow for better geometric overlap of laser beams and atomic cloud during the post-cooling phase (see below). After the drop, the light for loading and repumping is turned back on. The cold atoms are launched vertically by moving molasses. The moving molasses is created by simultaneous detuning of the three upper beams (using AOM_3) versus the three lower beams (using AOM_4). In a post-cooling phase after the launch, the atoms are additionally cooled by optimized polarization gradient cooling. The optical frequency of the molasses light is detuned ~ 68 MHz below the cycling transition, and the light intensity is simultaneously ramped down. The rates of frequency detuning and intensity ramping are tailored to obtain

the maximum number of detected atoms. The repumping laser is turned off several milliseconds after the molasses laser light to transfer all atoms into the $|F = 4\rangle$ state.

After 44 ms of flight, the atoms reach the state-selection cavity, where a microwave π-pulse transfers the atoms in the state $|4, 0\rangle$ to the $|3, 0\rangle$ state. The magnetic field in the state-selection cavity is oriented vertically which maximizes the probability for the $|4, 0\rangle \rightarrow |3, 0\rangle$ microwave transition for the given microwave field. The microwave field frequency in the state-selection cavity is tuned to the atomic microwave resonance only when the atoms pass through the cavity, and is far detuned otherwise.

The atoms reach the upper detection zone approximately 78 ms after being launched. In that zone, they are exposed to laser light tuned 2 MHz above the $|F = 4\rangle \rightarrow |F' = 5\rangle$ optical transition. Because of the running wave in the upper detection zone, the near-resonant light transfers momentum to the atoms in $|F = 4\rangle$, so that they are effectively removed from the interaction zone. A small amount of atoms is pumped to the $|F = 3\rangle$ state due to off-resonant hyperfine optical pumping. The atoms in the $|F = 3\rangle$ state are unaffected by the light.

The power in the Ramsey cavity is optimized so that on resonance a maximum number of atoms is transferred from the $|3, 0\rangle$ to the $|4, 0\rangle$ state. Such optimization results in a nominal π pulse area.

The detection light is turned on 10 ms before the atoms reach the upper detection zone. The frequency detuning of the detection light is different during the detection processes from the detuning during the pushing process. When the light frequency is tuned above resonance, the atoms are heated more effectively even in a standing wave configuration, and their number (and so the fluorescence signal) starts to drop sharply with increased blue detuning. To avoid fluctuations in the number of detected photons due to laser frequency excursions above the optical transition frequency, and in order to optimize the detected signal, the laser detuning is chosen to be 2 MHz below the $|F = 4\rangle \rightarrow |F' = 5\rangle$ transition. The magnetic field in the detection zone has been aligned with the vector $\vec{k}$ of the light (horizontal direction) in order to transfer the atoms into the $|4, 4\rangle$ component through Zeeman optical pumping. In this case, off-resonant hyperfine optical pumping is suppressed during the detection in the upper zone. The detection light intensity is $\sim 1\,\mathrm{mW/cm^2}$, resulting in $\sim 10^4$ scattered photons per atom during the flight through the detection zone.

After the number of atoms N_4 in the $|F = 4\rangle$ state has been detected by the standing wave part of the upper detection zone, they are removed from the cloud, and the number of atoms N_3 in the $|F = 4\rangle$ state is detected in the lower detection zone (see Section 2.2).

The ratio $S = N_4/(N_3 + N_4)$ is used to determine the transition probability due to the Ramsey microwave interaction. This normalization reduces the signal fluctuations due to shot-to-shot atom fluctuations [17]. A typical Ramsey fringe pattern is shown in Figure 3.

3. Frequency corrections and their uncertainty evaluation

The output of a primary frequency standard is subject to frequency biases. In order to realize the SI second according to its definition, corrections of the output frequency of the standard, corresponding to these frequency biases, must be applied. This section describes in detail the magnitude and the uncertainty of the corrections applied to the output frequency of CSF2.

3.1. Quadratic Zeeman effect

The largest correction to the frequency of the standard is associated with the second-order Zeeman shift. Between the two Ramsey interactions, the atoms travel in a region of nonzero axial magnetic field used to remove the degeneracy of the m_F Zeeman components belonging to the same ground state component F. This field causes a second-order Zeeman shift of the clock transition frequency. The Zeeman shift correction and its uncertainty is calculated from the measured value of the magnetic flux density B_c above the Ramsey cavity, averaged over the ballistic time of flight. The magnetic flux density B_c can be determined by a measurement of the linear Zeeman frequency shift of the magnetically sensitive components $|F, m_F \neq 0\rangle$ of the ground state. In practice, the Zeeman shift is measured by tuning the frequency of the microwave field in the Ramsey cavity to the $|4, -1\rangle \rightarrow |3, -1\rangle$ transition. In order to have a nonzero population of the $|4, -1\rangle$ state, the microwave field in the state-selection cavity and the pushing of the atoms on their way up are turned off. The frequency detuning f_{Z} of the $|4, -1\rangle \rightarrow |3, -1\rangle$ transition from the clock transition frequency f_0 is used for the calculation of B_c. The value of the magnetic flux density B_c, the Zeeman shift correction f_c of the clock transition frequency f_0, and the uncertainty of the shift correction δf_c are determined from the following formulas [21]:

$$
\begin{aligned}
B_c &= [f_{\mathrm{Z}}/\,(2 \times 3.5042)]\,\mu\mathrm{T}/\,\mathrm{kHz} \\
f_c &= -8 \times (f_{\mathrm{Z}}/f_0)^2 \\
\delta f_c &= 16 f_{\mathrm{Z}} \times \delta f_{\mathrm{Z}}/f_0^2
\end{aligned}
\tag{1}
$$

where $f_0 = 9\ 192\ 631\ 770\,\mathrm{Hz}$. The typical value of the frequency detuning f_{Z} is 1027.0 Hz. It corresponds to a ballistic flight-averaged magnetic flux density of 146.54 nT. The corresponding relative correction of the fountain clock transition frequency due to the second-order Zeeman shift is -99.85×10^{-15}.

The vertical profile of the amplitude of the magnetic flux density is measured by launching the atoms with different initial velocities, i. e. to correspondingly different apogee heights [22]. A magnetic field profile is then constructed by a deconvolution of the average magnetic field and the ballistic time of flight. The magnetic field profile

of the fountain is shown in Figure 4. It shows an inhomogeneity (standard deviation) of less than 0.2 nT. From this number we calculate an uncertainty of the second-order Zeeman shift due to the inhomogeneity of the B_c field of 2×10^{-19} [23]. The temporal instability of the magnetic field creates a larger uncertainty of the correction value. By repeated measurements over a period of months, a monthly variation of the value of f_Z of less than 0.3 Hz was found. Such variation corresponds to an uncertainty of the second-order Zeeman shift correction on the order of 0.06×10^{-15}.

3.2. Blackbody radiation shift

If the atoms are exposed to electromagnetic radiation during their ballistic flight between the two Ramsey interactions, the fountain output can be subject to an AC Stark shift [24]. One source of electromagnetic radiation is the blackbody radiation. The blackbody radiation shift of the output frequency of primary frequency standards has been extensively studied both experimentally and theoretically. At PTB, the CSF2 primary standard is located in a temperature-controlled environment, with annual peak-to-peak temperature variations on the order of 0.2 K. During the ballistic flight, the atoms are shielded from the external environment by the vacuum enclosure. The vacuum enclosure is made of copper, which provides an excellent uniform temperature distribution along the drift tube. Due to its rather low loaded Q-factor, the Ramsey microwave cavity does not have to be temperature-controlled and has the same temperature as the rest of the fountain structure. The optical molasses operation of the fountain avoids the use of magnetic field coils typically used in a magneto-optical trap (MOT) setup, and so local heating of the structure due to the coil current is absent.

The correction to the output frequency of the standard is based on the assumption that the radiation distribution is equivalent to that of a blackbody with temperature equal to the average temperature measured by the four PT100 sensors located along the drift tube. The calibration of the PT100 sensors provides an absolute temperature measurement uncertainty of 0.2 K. With a known value of the blackbody temperature, the blackbody shift δf is calculated using the formula [25]:

$$\delta f = k_0 E_{300}^2 \left(T/T_0\right)^4 \left(1 + \epsilon \left(T/T_0\right)^2\right) \tag{2}$$

where $k_0 = -2.282(4) \times 10^{-10}\,\mathrm{Hz/(V/m)^2}$ is the scalar DC polarizability of the clock transition [26], $E_{300} = 831.9\,\mathrm{V/m}$ is the *rms* electric field of the black body radiation at $T_0 = 300\,\mathrm{K}$ from Stefan-Boltzmann's law [25], T is the blackbody temperature in Kelvin, and the value of $\epsilon = 0.013(1)$ is based on a recent evaluation [27]. Using the average value of the temperature $T = 296.5\,\mathrm{K}$, assuming a measurement uncertainty of 0.2 K, and taking into account the uncertainty of k_0, the blackbody correction for CSF2 is calculated to be $16.60(6) \times 10^{-15}$.

3.3. Gravitational shift and relativistic Doppler shift

For comparisons with other clocks at different heights above the geoid and for contributions to TAI, the output of a primary frequency standard must be corrected for the gravitational shift. In a fountain, another much smaller relativistic effect – the relativistic Doppler effect – depends on the position-dependent atomic velocity during the ballistic flight. To correct the fountain frequency with an uncertainty of 1×10^{-16}, the ballistic flight-averaged height above the geoid must be known with an uncertainty of $\sim 0.9\,\mathrm{m}$. In a first step, the height of a reference point on the CSF2 support frame was determined in two independent ways, by standard surveying techniques relative to a known German reference point in the vicinity of PTB's clock hall, and by triangulation from the phase center of a GPS antenna mounted on the roof of the clock hall. The resulting ellipsoid height was converted into the height above the geoid using the European Gravimetric Quasigeoid Model EGG97 [28]. The time-averaged height of the atoms during their flight above the Ramsey cavity was then calculated using the known geometry data and launch velocity, and amounts to $h = 78.59(5)\,\mathrm{m}$. Using $g = 9.81252\,\mathrm{m/s^2}$ for the local total acceleration (gravitational and centrifugal), the corresponding correction $-hg/c^2$ of the clock transition frequency amounts to $-8.567(6) \times 10^{-15}$, where a small contribution by the relativistic Doppler effect of 1.4×10^{-17} is included.

3.4. Collisional shift

In general, collisions between the cold atoms in the cloud during their ballistic flight above the Ramsey cavity lead to a systematic shift of the fountain frequency [29]. The use of large-beam optical molasses in CSF2 results in a larger, less dense atom cloud with more uniform density distribution compared to fountains using a MOT. Thus, for the interrogation of the same number of atoms, the value of the collisional shift in CSF2 is reduced compared to fountains based on MOT loading or small-beam molasses.

The temperature of the atoms can be inferred from the change of their spatial distribution during their ascent and descent. Time of flight curves from the lower detection zone using a detection laser beam height of 1 mm are shown in Figure 5. The horizontal axis has been rescaled from detection time to position using the atomic velocity. From this data and the average vertical atom velocity of $v_0 = 3.73\,\mathrm{m/s}$ in the lower detection zone, the vertical radii of the cloud σ ($e^{-1/2}$) are determined to be 6.2 mm and 7.3 mm for the two time-of-flight curves, respectively. From these two measurements, a 1D temperature of the cloud of $T = 600\,\mathrm{nK}$ is inferred. The temperature and the initial cloud size are calculated from the formula for the expansion of a cloud with normal distribution of atomic velocities and positions: $\sigma(t) = \sqrt{\sigma(0)^2 + (\delta v \times t)^2}$, where $\delta v = \sqrt{k_B T / m_{\mathrm{Cs}}}$ is the standard deviation of the 1D velocity distribution of atoms with temperature T, k_B is the Boltzmann constant, m_{Cs} is the mass of the caesium atom, and t is the time of thermal expansion. In this calculation a small contribution from the detection laser beam height is neglected.

This simple model does not take into account the contribution of the laser beam size in the detection zone, and works only with the simplification of normally distributed velocities and atomic positions. Another method for cloud temperature determination is described in [30], where the temperature of the cloud is inferred from its expansion using deconvolution methods. The method does not neglect the detection beam size, and does not assume Gaussian position and velocity distributions. The temperature of the cloud can be determined by the width of the velocity distribution. Using the width of the deconvoluted velocity distribution obtained from the data shown in Fig. 5, the cloud temperature is found to be $T \approx 580(50)\,\mathrm{nK}$, in very good agreement with the simple model described in the previous paragraph. The cloud temperature is sensitive to the intensity balance of the molasses beams, and is calculated for each fountain cycle, showing a shot-to-shot variation of less than 10%. Because of the $(1, 1, 1)$ fountain geometry, the temperature of the cloud in the horizontal plane is expected to be the same as in the vertical direction. As a further confirmation of this rather low cloud temperature we note that the calculated loss of atoms due to the horizontal cloud expansion beyond the cutoff tube apertures is consistent with the measured loss of atoms derived from the time-of-flight curves (ascent and descent).

The collisional shift in CSF2 is measured by changing the density of the atomic cloud, and using the linear dependence of the shift versus atomic density [29, 31]. The way we change the atomic cloud density is by delaying the start of efficient molasses loading. The number of loaded atoms is controlled by opening shutter S_6 (controlling the repumping laser in the cooling zone) after a specific delay from the start of the cooling cycle. If during the cooling cycle the repumping laser is off, the atoms are effectively pumped into the $|F = 3\rangle$ state and cannot be cooled by the molasses. The shutter S_6 is opened 0.4 s or 1.6 s before the atoms are launched, respectively. For a collisional shift measurement CSF2 is switched between low and high atom number operation every 1000 s while the fountain output frequency is measured against two active hydrogen masers, of type Vremya-Ch VCH-1005 (BIPM clock code 1400590) and VCH-1003 (BIPM clock code 1400506), and designated H5 and H6. In order to keep the laser and AOM duty cycles the same, the cycle time is the same in both regimes. As a consequence the short-term stability at low atom densities is degraded due to the Dick effect. All other fountain parameters are also kept the same.

For the correction of the collisional shift for fountain evaluations we follow the procedure described in [4]: The collisional shift is measured before and after the frequency evaluation of the fountain. The value of the collisional shift slope is calculated from the collisional shift as a function of the detected atom number, as a weighted average of the two measurements. The measured average detected atom number during the evaluation period is used to calculate the collisional shift correction and its statistical uncertainty taking into account the statistical uncertainties of the collisional shift measurements. Additionally, a 10% systematic uncertainty is associated due to a potential change of cloud parameters between low and high density operation, and is added in quadrature to the statistical uncertainty. As a typical collisional shift correction

we obtain $-0.32(62) \times 10^{-15}$ for typical CSF2 operating conditions (500 ms loading time, total number of detected atoms $\sim 3 \times 10^4$).

Results of several collisional shift slope measurements are shown in Figure 6. Each point represents a mean value over at least 5 days of averaging. The data set spans a period of about one year. The measurements do not show any apparent drift.

The contribution of the collisional shift uncertainty to the uncertainty budget of the fountain is 0.62×10^{-15}, dominated by statistics. A slow-beam loading for CSF2 is planned for the near future, which will significantly increase the number of detected atoms, and thus the collisional shift. In this case, the systematic uncertainty due to the change of the cloud parameters will be more significant, and the rapid adiabatic passage method [12] will be used in order to reduce it below the 1% level.

4. Further systematic uncertainties and their evaluation

4.1. Light shift

In general, the presence of near-resonant laser light causes a frequency shift of the clock transition. Several mechanisms are implemented in CSF2 in order to reduce the magnitude of this light shift. First, the RF power sent to the acoustooptic modulators (AOM_3, AOM_4, AOM_5 and AOM_6) is switched off between the two Ramsey interactions. Additionally, shutters S_3 to S_6 block the laser beams entering the optical fibers which deliver the light to the fountain structure. The residual amount of light at the output of the optical fibers with the AOMs off and shutters closed was below 0.01 nW, limited by the sensitivity of the power detector. The extinction ratios of the acoustooptic modulators and shutters, determined by the residual amount of light leaking behind them into the optical fibers, were better than 3×10^{-7}, limited by the sensitivity of the power detector. This was confirmed by making sure that there is no change of the power meter reading when the laser beams were additionally manually blocked in front of the optical fiber inputs. Another mechanism used to suppress the light shift is the closing of shutter S_2 during the ballistic flight of the atoms, which causes the two slave lasers to operate in a free-running mode at wavelengths detuned by more than a nanometer from the Cs D_2 transition at 852 nm.

In order to evaluate the magnitude of the light shift due to the laser light, CSF2 was operated in special modes as described below. First, the detection light was switched on during the ballistic flight by leaving AOM_5 and AOM_6 on. The shutters S_2, S_5 and S_6 were left open. The frequency of CSF2 was measured against the two masers H5 and H6. Then, the shutters and the AOMs were operated normally, and the CSF2 frequency was again measured against H5 and H6. The effect of the drift of the maser frequencies was reduced by measurements under nominal conditions before and after the light shift evaluation measurement. The change of the frequency of CSF2 in the presence of stray light from the detection zone was measured to be on the order of 20×10^{-15}. Second, the molasses laser light was turned on by switching on the acoustooptic modulators

AOM_2, AOM_3 and AOM_4, and leaving shutters S_2, S_3 and S_4 open during the atomic ballistic flight after the apogee. The maser drift was again removed by measuring the frequency of CSF2 under nominal conditions before and after the light shift evaluation measurement. The change of the frequency of CSF2 in the presence of molasses laser light leaking into the drift tube was measured to be 1100×10^{-15}.

When the shutter S_2 is left open, the two slave lasers remain injection-locked between the two Ramsey interactions. Thus, if there was any light present in the drift zone during the ballistic flight, the light shift value would change in this case. Experimentally, no frequency change at the level of 2×10^{-15} (limited by the statistical resolution of the measurement) was observed when shutter S_2 was left open or closed during the ballistic flight.

Considering the light extinction ratios given above, the light shift is estimated to be well below the 10^{-18} level. No light shift correction is applied to the fountain frequency.

4.2. Cavity phase shift

The accuracy of any frequency standard based on a two-zone Ramsey interaction suffers from microwave phase shifts between the two interactions. Due to the fountain geometry the same microwave field is used for the two Ramsey interactions. The advantage is that if the atoms pass through the cavity twice at exactly the same position, any radial or axial cavity phase variation will not produce a shift of the clock frequency.

However, the size of the cloud leads to atoms passing on their way up at different radial positions of the cavity. Moreover, an atom does not cross the microwave cavity at the same position during its second passage in general because of the nonzero temperature and because of a possible misalignment of the launch direction with respect to the vertical. Thus, a spatial phase variation of the microwave field can lead to a shift of the frequency of the standard. For the evaluation of possible resulting frequency shifts of CSF2 we use the same approach as was used for the evaluation of CSF1 [3]. As mentioned, the Ramsey cavity used in CSF2 is identical in design to the cavity used in CSF1 [19].

Due to the relatively strong coupling, resulting in a low loaded Q of our cavities, the measured resonance frequency is shifted by $-20\,\mathrm{MHz}$ with respect to the resonance frequency calculated by using the diameter and the height of the cavity. The actual microwave field in the cavity can be described by a superposition of various field modes TE_{npq} that are excited with different amplitudes and phases [32]. The model describes the field in the cavity to consist of a dominant TE_{011} mode with losses, and other contributing modes which have no losses. Depending on the location of their resonance frequencies with respect to the excitation field frequency, the phases of the other contributing modes are either at 90° or -90° with respect to the exciting field phase. By contrast, at the shifted resonance frequency of the actual microwave field in the cavity the phase ϕ_{011} of the dominant TE_{011} mode is calculated to be shifted by less than 1° with respect to the modes exhibiting a 90° phase, when the $-20\,\mathrm{MHz}$-shift

and the quality factor of the TE_{011} mode ($Q_r \approx 28000$) is taken into account. As a result the actual microwave field in the cavity at resonance is nearly in phase or 180° out of phase to all other modes. From the small phase difference $\phi_{011} < 1°$ and from the calculated coupling strength of the other modes the phase of the resulting field and its spatial variation can be calculated by vectorial addition of the respective phasors of the field modes and taking into account the spatial variation of each field mode.

We only consider contributions by the TE_{npq} modes which can be excited by the two coupling slits in our cavity and whose resonance frequencies are close to the TE_{011} mode resonance frequency. For perfectly symmetric coupling at the two coupling slits, only TE_{n11} modes with n even can be supported by the cavity. The mode with the closest resonance frequency is the TE_{211} mode, which gives rise to an approximately quadratic phase dependence in the horizontal plane around the cavity axis. In the case of asymmetric coupling TE_{n11} modes with n odd can be excited in the Ramsey cavity, too. In this case we take into account a superposition of the contributions of the TE_{111} and the TE_{311} mode, which again are closest in the resonance frequency. Both latter contributions together give rise to a complicated phase variation around the cavity axis exhibiting a saddle point on the axis.

Because the cavity apertures for the atoms are centered on the cavity axis, it is guaranteed that all detected atoms were only exposed to the field around the cavity axis within a diameter of 10 mm. Because all distortion modes considered exhibit comparably small longitudinal H-field components close to the cavity axis when the superposition with the strong longitudinal H-field of the TE_{011} field is considered, the resulting calculated phase variations in the region of interest around the cavity axis are at most at the micro-radian level.

The outlined behavior of the cavity phase across the opening of the Ramsey cavity is used to estimate the average phase shift the atoms can experience as their position changes between the first and the second passage through the cavity. The estimation is done using a Monte-Carlo simulation of the ballistic flight of the atomic cloud. In the simulation it is assumed that the initial positions and velocities of the atoms correspond to normal distributions determined by a cloud radius of 6 mm ($e^{-1/2}$) and a temperature of $T = 0.6\,\mu$K. The atom cloud center is allowed to have an initial radial offset as the cloud enters the cavity, and to propagate at an angle with respect to the vertical. The average radial position offset and the vertical misalignment are chosen in the direction of maximum phase gradient. For the case of the TE_{211} mode, the average initial position offset is set to zero, since the phase dependence is radially symmetric. For the case of the TE_{111} and the TE_{311} mode, the phase changes sign for opposite displacements from the cavity center, and thus may add up for the atoms on their way up and down. Therefore in the simulation the average radial offsets are chosen to have the same magnitudes, but opposite signs for the two cavity passages. The maximum angle with respect to the vertical is restricted in order to have at least 30% of the atoms back in the detection zone after the second passage. This is the fraction of returning atoms that has been determined experimentally before.

For the case of perfectly symmetric coupling, i.e., the TE_{211} mode contributing only, we find that the maximum average relative frequency shift is 0.07×10^{-15}. On the other hand, assuming an asymmetric coupling by the utilization of a single coupling slit only, the maximum relative frequency shift due to the TE_{111} and the TE_{311} modes is calculated to be 0.75×10^{-15}. Thus we obtain for a worst-case assumption of a 10% coupling asymmetry between the two slits that the resulting maximum average frequency shift is 0.075×10^{-15}. Adding both symmetric and asymmetric contributions results in a possible frequency shift of 0.15×10^{-15} due to the distributed cavity phase. This value is taken as the uncertainty of the total distributed cavity phase shift.

4.3. Majorana transitions

When an atom enters a region of a zero or a rapidly changing magnetic field, it can experience Majorana transitions which will transfer it into a new superposition of atomic states [33]. In the case of a fountain clock, changes in the magnetic field during the ballistic flight of the atoms may transfer an atom prepared in the state $|F, m_F = 0\rangle$ into a superposition of $|F, m_F\rangle$ states. Depending on the detailed geometry of the fountain this can happen between the atomic state preparation and the first Ramsey interaction and/or between the second Ramsey interaction and the detection, whereas between the Ramsey interactions such transitions are generally avoided by the homogeneous B_c-field. Majorana transitions which happen before the atomic state preparation are not harmful because of the state selection process.

Frequency shifts, which occur due to Majorana transitions in combination with $\Delta F = 1, \Delta m_F = \pm 1$ transitions in the Ramsey cavity, have been observed and investigated in the past [34, 35]. The latter transitions are possible only if the magnetic field inside the Ramsey cavity is not parallel to the field lines of the magnetic flux density B_c. Because of the curvature of the TEM_{011} microwave field lines, atoms which do not travel exactly along the axis of the cavity have a finite probability to undergo $\Delta m_F = \pm 1$ transitions, even if the magnetic field and the axis of the cavity is perfectly aligned.

In order to check for the presence of Majorana transitions in CSF2, the local magnetic field along the atomic trajectory above the cooling zone was mapped using the atoms as a magnetically sensitive probe. The mapping was done using transitions between Zeeman substates belonging to the same ground state hyperfine component (Zeeman transition measurements), and using magnetic field-sensitive hyperfine transitions between Zeeman substates belonging to different ground state components (hyperfine transition measurements).

For the Zeeman transition measurements, the fountain was operated with state-selection. The microwave field in the Ramsey cavity was referenced to one of PTB's masers and was tuned on resonance. This configuration resulted in 95% of the atoms being transferred from $|3, 0\rangle$ to $|4, 0\rangle$ by the Ramsey interaction. At a specific time delay after the state selection, a 5 ms long RF-pulse (with frequency in the kilohertz range)

was applied using a set of coils outside the vacuum system. The delay of the pulse was selected to correspond to a certain position of the atoms above the state-selection cavity. For each delay, the frequency of the pulse was varied between 5 kHz and 200 kHz. When the frequency of the pulse matched the Larmor frequency $f_L = 3.5042 \times B\,(\mathrm{kHz}/\mu\mathrm{T})$ of the atoms, the applied pulse transferred some of the atoms from $m_F = 0$ to the $m_F = \pm 1$ states, leaving them unaffected by the following Ramsey microwave interaction. Because of that, the number of atoms transferred to $|4, 0\rangle$ was reduced. The amplitude of the pulse was adjusted to minimize the number of atoms transferred to $|4, 0\rangle$. The frequency of the pulse which minimized the number of atoms transferred to $|4, 0\rangle$ was used to calculate the magnetic flux density at the specific height using the expression for the Larmor frequency. The magnetic field mapping was performed for heights starting at the state-selection cavity up to the bottom end of the outer layer of the magnetic shields (see Fig. 1); above this height the shields prevent the low-frequency field from penetrating inside and exciting Zeeman transitions. A map of the magnetic field is shown in Fig. 7 (open triangles).

For the hyperfine transition measurements, an RF-pulse of 5 ms length and with a variable delay with respect to the time of the launch of the atoms was applied using a microwave horn mounted close to the detection zone. In order to increase the spatial resolution, the vertical Gaussian radius of the cloud was reduced to ~ 3 mm ($e^{-1/2}$) by using a short pushing pulse in the detection zone which removed the atoms at the top of the cloud. The RF pulse caused hyperfine transitions between different Zeeman sublevels of the two ground state components. Due to the uncontrolled polarization state of the RF field, it caused $\Delta m_F = 0, \pm 1$ transitions when the RF frequency matched the transition frequency between the Zeeman sublevels. By choosing the delay, the RF frequencies at which the transitions $m_F = 0 \rightarrow m_F = \pm 1$ occurred were used to calculate the magnetic field at the corresponding atom position (Figure 7, open circles). Due to the cutoff tubes, no signal was obtained within the state-selection cavity, the Ramsey cavity and the tubes themselves. The positions of the cavities and the three magnetic shields are indicated in Figure 7, as well. The Zeeman and hyperfine transition measurements show agreement with each other. Note that on the scale of Figure 7 the highly homogeneous field above the Ramsey cavity (Figure 4) looks completely flat.

It is clear from the measurements that the atoms do not cross a point of zero magnetic flux density along their trajectory. A detailed analysis of the measurements including the effect of the cloud size and microwave pulse length was performed, verifying this conclusion. The weak-field adiabatic condition [21] is satisfied everywhere to at least 2×10^{-2}, assuming a worst-case $\pi/2$-angle between the quantization field and the direction of the field gradient. Under the same assumption for the angle, a calculation of the probability for Majorana transitions in the region of strong magnetic field gradients has been performed. The calculation shows that the residual populations of $m_F = \pm 1$ states due to Majorana transitions are on the order of 5.0×10^{-6} from that of the $m_F = 0$ state, resulting in a frequency shift below 1.0×10^{-19}.

4.4. Rabi and Ramsey pulling

The Rabi pulling shift is due to the presence of a sloping background in the vicinity of the central Ramsey fringe. The interaction with the microwave field during the state selection process and the subsequent pushing by laser light causes a small portion of the atoms to end up in $|3, m_F \neq 0\rangle$ substates. Subsequently, the microwave field in the Ramsey cavity can cause $\Delta m_F = 0$ transitions into states $|4, m_F \neq 0\rangle$. The Rabi pedestals of these transitions create a sloping background in the transition probability when the populations of $|3, +m_F\rangle$ and $|3, -m_F\rangle$ states are not equal.

The largest contribution to Rabi pulling comes from the $\Delta m_F = 0$ transitions between $|m_F| = 1$ states, because their transition frequencies are closest to the clock transition frequency. By exciting $\Delta m_F = 0$ transitions $|3, m_F = 0, \pm 1\rangle \rightarrow |4, m_F = 0, \pm 1\rangle$, the populations of the $|3, m_F = \pm 1\rangle$ states in CSF2 are measured to be 0.25% of that of the $|3, m_F = 0\rangle$ state. At the same time the population imbalance of the $|3, m_F = \pm 1\rangle$ states is determined to be $|(p_{1,1} - p_{-1,-1}) / (p_{1,1} + p_{-1,-1})| = 2.5 \times 10^{-2}$, where $p_{1,1}$ and $p_{-1,-1}$ are the populations of the $|3, m_F = +1\rangle$ and $|3, m_F = -1\rangle$ states, respectively. For a typical detuning of 1 kHz of the $\Delta m_F = 0$ transitions $|3, m_F = \pm 1\rangle \rightarrow |4, m_F = \pm 1\rangle$ from the clock transition frequency, the corresponding Rabi pulling shift is calculated to be 1.5×10^{-19} using the theory outlined in [36].

In a fountain, Ramsey pulling is mainly due to the presence of $\Delta m_F = \pm 1$ transitions $|3, m_F = 0\rangle \rightarrow |4, m_F = \pm 1\rangle$ and $|3, m_F = \pm 1\rangle \rightarrow |4, m_F = 0\rangle$ in the Ramsey cavity. These transitions can be observed by measuring the ratio $S = N4/(N3+N4)$ as a function of the detuning of the microwave frequency in the Ramsey cavity in the vicinity of $f_{\mathrm{Z}}/2$. In CSF2, the maximum of the ratio S is on the order of 0.7% relative to the clock transition probability on resonance and can be attributed to the first kind of transitions only, because the population of the $|3, m_F = \pm 1\rangle$ states is small due to the state selection (see above). The asymmetry between the $|3, m_F = 0\rangle \rightarrow |4, m_F = +1\rangle\,(\oplus)$ and the $|3, m_F = 0\rangle \rightarrow |4, m_F = -1\rangle\,(\ominus)$ transitions, can be defined as the ratio $|(S(\oplus) - S(\ominus)) / (S(\oplus) + S(\ominus))|$, where $S(\oplus)$ and $S(\ominus)$ are the maxima of S for the $\oplus$- and $\ominus$-transitions, respectively. It was found to be $1.0(0.4) \times 10^{-3}$. No change of this ratio was found, when in the detection zone σ^+ or σ^- laser light polarization was used, in order to estimate an alleged probability imbalance due to the detection process. Using the results from [36], the magnitude of the Ramsey pulling shift for such a transition probability imbalance is calculated to be less than 1.0×10^{-19}.

Even though the $|3, m_F = \pm 1\rangle$ states are only weakly populated, they are more probable to entail an asymmetry due to the state selection process, resulting in frequency shifts due to Ramsey pulling. As already stated above, in CSF2 the population asymmetry is measured to be less than 2.5×10^{-2}. Again using the results from [36], the magnitude of the resulting shift for such a population asymmetry is calculated to be less than 1.0×10^{-18}, which is taken as the overall uncertainty contribution for Ramsey pulling.

4.5. Shifts due to the electronics

It had been pointed out already that for continuous caesium beam atomic clocks, the presence of spurious spectral microwave components with frequencies different from that of the clock transition, i.e., asymmetric sidebands in the microwave spectrum, distort the Ramsey resonance curve, thus leading to a frequency bias of the microwave frequency standard output [37, 21].

For the currently employed frequency synthesis for CSF2, the largest frequency components present in the microwave signal sent to the Ramsey cavity are 100 Hz sidebands on the 9.192 GHz carrier. We find these sidebands to be at -50 dB below the carrier. Assuming a 10% amplitude asymmetry of the sidebands we obtain a frequency shift at nominal microwave power (see section 4.7) of less than 0.17×10^{-15} using the theory developed in [37].

It also had been pointed out theoretically and experimentally that in continuous beam atomic clocks a modulation which is synchronous with a sideband frequency may result in large frequency shifts [20]. Corresponding investigations for a fountain standard [38] revealed possible frequency shifts much larger than the shift mentioned above, which is just due to asymmetric sidebands. In CSF2 the cycle time (1.395 s) is chosen such that the fountain cycle has the same phase with respect to the 100 Hz period every two shots. Thus, the phase of the spur component for each cycle has an additional π phase difference with respect to the previous cycle. In this case no frequency shift at the 10^{-17} level is expected due to averaging over 2 cycles, and we can neglect this effect compared to the effect discussed above. It should also be noted that in CSF2 there is no common frequency reference for the microwave frequency modulation and the synthesized microwave radiation. In the near future a new frequency synthesis setup [39] with an improved performance will be utilized for CSF2. It has already been demonstrated that utilizing the new synthesis together with a better magnetic shielding of the quartz oscillator results in a much better suppression of sidebands.

Another potential and systematic shift could result from a reproducible and systematic variation of the efficiency of measuring $S = N_4/(N_3 + N_4)$ from cycle to cycle, e.g., due to 50 Hz distortions of the detection signal. However, the choice of the cycle time (1.395 s) also cancels out this kind of synchronous shift due to averaging over 4 cycles. From further experimental investigations we expect to obtain a more stringent limit on the related shifts.

Systematic errors arising from a potential quadratic frequency drift of the quartz oscillator and a linear drift of the offset of the operational amplifier in the analog integrator (see section 2.4) are expected to contribute less than 0.1×10^{-15} in relative units. This estimate is based on experimental findings and the specifications of the individual components. The total contribution of the electronics to the CSF2 uncertainty budget is thus 0.2×10^{-15}.

4.6. Microwave leakage

In general, the existence of microwave leakage results in frequency shifts [40, 41]. In order to search for any leakage the microwave power inside the Ramsey cavity was increased to about 1 W (65 dB higher than normal). No microwave power larger than -153 dBm (the sensitivity limit of our spectrum analyzer) can be picked up with a microwave horn antenna anywhere in the vicinity of the fountain or the electronic subsystem. This test was also performed in the early stages of the construction of CSF2, before the vacuum system was closed, so that the leakage search could be performed directly at the Ramsey cavity and its feeds. Similar tests did not reveal any leakage from the state selection cavity, which moreover is far detuned during each cycle, once the state selection has been performed. We thus conclude from the results of our investigations about the effects of microwave leakage [40] that any associated shift is well below the 10^{-16}-level and attribute a corresponding uncertainty. For the near future, in order to corroborate this finding, we plan further investigations using a microwave switch free of phase transients as has been developed and demonstrated recently [42].

4.7. Microwave power shift

It is well known that in fountain frequency standards frequency differences may be observed when operating the standard at normal optimized microwave power or at elevated microwave power levels. For the origin of such frequency differences a number of effects, discussed in Sections 3.4, 4.2, 4.3, 4.4, 4.5, 4.6, come into consideration: cold collisions, cavity phase shifts, Majorana transitions, Rabi and Ramsey pulling, spurious microwave components, and microwave leakage. Experiments with PTB's first caesium frequency fountain CSF1 revealed the presence of power-related frequency shifts [43]. Experiments with elevated microwave power in CSF2 were also performed, and the results are outlined below.

When the microwave power in the Ramsey cavity is varied, the pulse area the atoms experience as they pass through the cavity is changed. A π microwave pulse causes an atom to undergo a full transition from one atomic hyperfine state to another. This definition can be extended to include $n\pi$ pulse areas (with n an odd integer), which leaves the atom in the same final state as at π pulse area, but with the amplitude of the microwave field n times higher. In an atomic fountain, atoms with different initial positions, launch directions and velocities are exposed to different microwave pulse areas due to the spatial profile of the microwave field inside the cavity. A nominal $n\pi$ pulse area is determined by measuring the microwave power at which there is the maximum probability for the ensemble of atoms to undergo the microwave transition. Depending on the order n of the $n\pi$ pulse, this approach leads to different state compositions of the coherent ground state superposition $a\,|3,0\rangle + b\,|4,0\rangle$ after the first Ramsey interaction, determined by the complex numbers a and b [44, 43]. In turn, a dependence of the collisional shift on the state composition [13] contributes to the fountain frequency dependence on the microwave power [44, 43].

For CSF2, in order to eliminate any varying collisional shift contribution to the measured power-dependent frequency shift, the area of each nominal $n\pi$ microwave pulse was adjusted to produce the same state composition after the first Ramsey interaction. The adjustment was done by measuring this state composition $(a\,|3,0\rangle + b\,|4,0\rangle)$, and keeping the ratio $|a/b|$ the same [43] for each nominal $n\pi$ microwave pulse measurement. The frequency shift versus microwave pulse area was determined by performing a differential frequency measurement of the fountain operating with 1π and $n\pi$ pulse areas, where the pulse area is switched every 1000 s. The two modes of operation were controlled by a voltage-controlled attenuator. Once the two microwave pulse areas were adjusted, the fountain was locked to the clock transition, while a phase comparator measured the phase difference between CSF2 and a stable maser reference. The observed microwave power-dependent frequency shift is shown in Figure 8.

From our investigations related to the effects of cold collisions, Majorana transitions, Rabi and Ramsey pulling, spurious microwave components and microwave leakage (see Sections 3.4, 4.3, 4.4, 4.5, 4.6), we conclude that any of these effects is highly unlikely to cause the observed microwave power dependence of the fountain frequency shift. Currently more work is in progress investigating whether the observed power-dependent shifts can be explained by longitudinal phase gradients caused by the cavity end-caps. In this case the frequency shifting effect for the nominal 1π pulse area operation may well be negligible [45].

To reflect our uncertainty as to whether the mechanism leading to the observed microwave power dependence (Fig. 8) also causes a frequency bias for normal operation at 1π pulse area we add a contribution to the uncertainty budget. As we have done previously in the case of CSF1, we use half of the frequency shift between 1π and 3π nominal pulse area operation as an estimate for the potential magnitude of a frequency bias. For CSF2, this difference is $0.79(48) \times 10^{-15}$, giving a contribution of 0.40×10^{-15} to the uncertainty budget.

4.8. Background gas pressure shift

The background gas pressure in CSF2 is reduced by the two ion pumps below and above the vacuum structure (see Fig. 1). The pressure of the residual gas in the drift tube of CSF2 is on the order of 5×10^{-8} Pa, estimated from the current reading of the top ion pump. Considering this to be the residual hydrogen pressure which would cause the largest frequency shift, the estimated uncertainty of the CSF2 frequency due to background gas collisions is less than 4.6×10^{-17} [21]. As a further corroboration that collisions with background gas atoms can be neglected, the number of atoms during their ascent and descent was derived from the time-of-flight measurements. The comparison shows that the fraction of atoms detected after their ballistic flight is consistent with the geometrical losses at the apertures of the cavities for the measured cloud temperature.

Table 1. Uncertainty budget of CSF2: Frequency shift type (origin), applied frequency correction, and frequency correction uncertainty (parts in 10^{15}).

Frequency shift	Correction	Uncertainty
Quadratic Zeeman shift	−99.85	0.06
Blackbody radiation shift	16.60	0.06
Gravity + relativistic Doppler effect	− 8.567	0.006
Collisional shift	0.32	0.62
Cavity phase shift	0.0	0.15
Light shift	0.0	0.001
Majorana transitions	0.0	0.0001
Rabi pulling	0.0	0.0002
Ramsey pulling	0.0	0.001
Electronics	0.0	0.20
Microwave leakage	0.0	0.10
Microwave power dependence	0.0	0.40
Background pressure	0.0	0.05
total	−91.50	0.80

5. Compilation of frequency corrections and systematic uncertainty contributions

The uncertainty budget of CSF2 together with typically applied corrections is given in Table 1. The depicted uncertainty budget is valid for designated frequency evaluations. Some uncertainty entries (quadratic Zeeman shift, collisional shift, microwave power dependence) are subject to change depending on the results of updated related evaluations. Such evaluations are performed for each individual CSF2 contribution to TAI calibrations. It should be noted that the currently dominating uncertainty contribution due to collisions is essentially given by the statistical uncertainty of related measurements and will be probably reduced along with future evaluations. Concerning the second largest contribution due to the microwave power dependence, work is in progress to clarify its origin and characteristics.

6. Performance of CSF2

Since the completion of CSF2, several frequency comparisons with the fountain CSF1 and the hydrogen masers at PTB were made using a phase comparator. The frequency measurements demonstrated a typical short-term instability of $2.5 \times 10^{-13}\,(\tau/\mathrm{s})^{-1/2}$ against the masers. The short-term instability is determined mainly by the combination of quantum projection noise and the Dick effect [46]. In the absence of microwave oscillator noise, the short-term instability of the fountain can be calculated from the

following expression for the Allan deviation [47]:

$$\sigma_y(\tau) = \frac{1}{\pi\, Q_{\mathrm{at}}\, S/N}\sqrt{\frac{T_c}{\tau}} \tag{3}$$

where $Q_{\mathrm{at}} = f_0/\Delta f$ is the atom quality factor, $f_0 = 9\,192\,631\,770\,\mathrm{Hz}$, Δf is the width of the Ramsey fringe, τ is the measurement time and T_c is the cycle time.

The signal-to-noise ratio S/N is determined by measuring $S = N_4/(N_3 + N_4)$ and its Allan standard deviation σ_A^S as the measure for the noise N for a range of molasses loading times. Changing the molasses loading time results in a variation of the launched and detected atom number (and evidently in a change of the cycle time T_c). To avoid the contribution from microwave oscillator noise, N was determined by setting the microwave power inside the Ramsey cavity to correspond to $2 \times \pi/4$ pulse area, with the microwave frequency kept at resonance. This pulse sequence leaves the atoms in an equal superposition of $|F = 3\rangle$ and $|F = 4\rangle$ states after the Ramsey interaction. As the observed signal-to-noise ratios are proportional to the square-root of the detected atom number signal, and as noise contributions from the photon shot noise are negligible, this measurement reveals quantum projection noise-limited performance [47]. This finding enables us to calculate the detected atom number as the square of the measured signal-to-noise ratios [10, 22]. From the signal-to-noise ratios, the expected short-term instability of the fountain due to the quantum projection noise at different cycle times was calculated (Fig. 9). The contribution from the Dick effect to the frequency instability has been calculated using the noise properties of the quartz interrogation oscillator as given in its datasheet and is also shown in Figure 9. The two contributions to the frequency instability have been added in quadrature to obtain the solid line in Figure 9. The actual frequency instability of CSF2 with respect to PTB maser H6 is shown by circles.

The best performance is predicted for $\sim 500\,\mathrm{ms}$ molasses loading time, corresponding to 1.395 s fountain cycle time. Figure 10 (open circles) illustrates the relative frequency instability against the maser H6, expressed by the Allan standard deviation $\sigma_y(\tau)$. For averaging times below $10^4\,\mathrm{s}$, the frequency instability is $\sigma_y(\tau) = 2.5 \times 10^{-13}\,(\tau/\mathrm{s})^{-1/2}$. For averaging times larger than $10^4\,\mathrm{s}$ the frequency drift of the maser is the limiting factor for the CSF2 instability measurement. The solid circles in Figure 10 show the relative frequency instability of CSF2 versus CSF1 over a 20-day period. The data points correspond to an instability $\sigma_y(\tau) = 2.8 \times 10^{-13}\,(\tau/\mathrm{s})^{-1/2}$, which is expected taking into account a $\sigma_y(\tau) = 1.3 \times 10^{-13}\,(\tau/\mathrm{s})^{-1/2}$ instability contribution by CSF1. Based on this result, we use $u_A = 0.7 \times 10^{-15}$ as an upper limit for the statistical uncertainty of CSF2 frequency measurements until further verification of the $\tau^{-1/2}$-dependence of the instability for long averaging times. This procedure is held likewise for measurements of the TAI scale unit.

The results of frequency comparisons between CSF2 and CSF1 are shown in Figure 11. The comparisons made between August 2008 and November 2008 (open circles) were done before the evaluation of most of the uncertainties given in Table 1.

The error bars shown for these data points are only the statistical uncertainties of the measurements. For each fountain, the output frequencies were corrected for second-order Zeeman shift, blackbody shift, gravitational shift and collisional shift. For the comparisons after December 2008, a systematic uncertainty evaluation was available. The error bars of this data are calculated as a quadrature of the statistical uncertainty of the measurement (limited to 0.7×10^{-15}), the total uncertainty of CSF2 according to Table 1, and the total uncertainty of CSF1. Both fountains agree with each other within the combined uncertainties. However, there seems to be a systematic offset of $\sim 1 \times 10^{-15}$ between the two devices, which requires further investigations.

Four informal frequency evaluations of CSF2 were reported to the Bureau International des Poids et Mesures (BIPM) between December 2008 and August 2009. The frequency of CSF2 with respect to the other fountain frequency standards regularly contributing data to the BIPM is shown in Fig. 12. The error bars comprise the statistical and systematic uncertainties of the standards and the uncertainties due to the link to TAI as given in the CircularT [48]. One can see that the CSF2 results appear to fall well within the range of results of the other primary frequency standards.

7. Conclusions

A first evaluation of the uncertainty of the second atomic fountain CSF2 at PTB has been performed. Under normal operating conditions, about 10^6 atoms cooled to $0.6\,\mu$K in a cloud of $\sim 6\,$mm ($e^{-1/2}$) radius are launched vertically from the cooling zone at $\sim 4.4\,$m/s. About 10% of them are prepared in the $|3,0\rangle$ state by the state-selection process. After the Ramsey interaction, 30% of these atoms ($\sim 3 \times 10^4$) are detected and provide information on the detuning of the microwave frequency from the atomic resonance. The fountain operates with a cycle time which minimizes the contributions from quantum projection noise and the Dick effect, resulting in a frequency instability $\sigma_y(\tau) = 2.5 \times 10^{-13}\,(\tau/\mathrm{s})^{-1/2}$. The systematic uncertainty of the frequency of the standard is 0.80×10^{-15}. The largest contributions to the uncertainty budget come from the collisional shift evaluation and a microwave power related effect. The use of large molasses laser beam diameters results in reduced shifts due to cold collisions. It is expected that with the implementation of a slow beam for molasses loading [2], the utilization of a new frequency synthesis setup [39] and a femtosecond laser microwave oscillator [10], the short-term instability of the fountain will be further reduced, and that the cold collisions shift value will be determined with better accuracy using the rapid adiabatic passage method [12].

Acknowledgments

The authors would like to thank Chr. Richter for the considerable support with the electronics, and B. Riedel of the Institut für Geodäsie und Photogrammetrie of the Technische Universität Braunschweig for the determination of the height of PTB's

clock hall above the geoid. We also would like to thank G. Panfilo of the staff of the BIPM Time Section for providing valuable comparison data between CSF2 and TAI. We gratefully acknowledge critical reading of the manuscript and valuable suggestions by A. Bauch. N. Nemitz is supported by a grant from DFG.

References

[1] R Wynands and S Weyers. *Metrologia*, 42(3):S64–S79, 2005.

[2] C. Vian, P. Rosenbusch, H. Marion, S. Bize, L. Cacciapuoti, S. Zhang, M. Abgrall, D. Chambon, I. Maksimovic, P. Laurent, G. Santarelli, A. Clairon, A. Luiten, M. Tobar, and C. Salomon. *IEEE Transactions on Instrumentation and Measurement*, 54(2):833–836, 2005.

[3] S. Weyers, U. Hübner, R. Schröder, Chr. Tamm, and A. Bauch. *Metrologia*, 38(3):343–352, 2001.

[4] S. Weyers, A. Bauch, R. Schröder, and C. Tamm. In *Proceedings of the 6th Symposium of Frequency Standards and Metrology*, pages 64–71, 2002.

[5] T. P. Heavner, S. R. Jefferts, E. A. Donley, J. H. Shirley, and T. E. Parker. *Metrologia*, 42:411–422, 2005.

[6] F. Levi, D. Calonico, L. Lorini, and A. Godone. *Metrologia*, 43:545–555, 2006.

[7] K. Szymaniec, W. Chalupczak, P. B. Whibberley, S. N. Lea, and D. Henderson. *Metrologia*, 42:49–57, 2005.

[8] T. Kurosu, Y. Fukuyama, Y. Koga, and K. Abe. *IEEE Transactions on Instrumentation and Measurement*, 53(2):466–471, 2004.

[9] M. Kumagai, H. Ito, M. Kajita, and M. Hosokawa. *Metrologia*, 45:139–148, 2008.

[10] S. Weyers, B. Lipphardt, and H. Schnatz. *Physical Review A*, 79:031803(R), 2009.

[11] J. Millo, M. Abgrall, M. Lours, E. M. L. English, H. Jiang, J. Guéna, A. Clairon, M. E. Tobar, S. Bize, Y. Le Coq, and G. Santarelli. *Applied Physics Letters*, 94:141105, 2009.

[12] F. Pereira Dos Santos, H. Marion, S. Bize, Y. Sortais, A. Clairon, and C. Salomon. *Physical Review Letters*, 89(23):233004, 2002.

[13] K. Szymaniec, W. Chalupczak, E. Tiesinga, C. J. Williams, S. Weyers, and R. Wynands. *Physical Review Letters*, 98:153002, 2007.

[14] S. R. Jefferts, T. P. Heavner, T. E. Parker, and J. H. Shirley. *Acta Physica Polonica A*, 112(5):759–767, 2007.

[15] D. Calonico, F Levi, C. E. Calosso, E. K. Bertacco, G. Costanzo, and A. Godone. In *Proceedings of the 7th Symposium of Frequency Standards and Metrology*, pages 228–232, 2008.

[16] R. Wynands, D. Griebsch, R. Schröder, and S. Weyers. In *Proceedings 20th European Frequency and Time Forum*, pages 200–202, 2006.

[17] A. Clairon, S. Ghezali, G. Santarelli, Ph. Laurent, S. N. Lea, M. Bahoura, E. Simon, S. Weyers, and K. Szymaniec. In *Proceedings of the 5th Symposium on Frequency Standards and Metrology*, pages 45–59, 1996.

[18] R. Schröder and U. Hübner. In *Proceedings of the 14th European Frequency and Time Forum*, pages 480–484, 2000.

[19] R. Schröder, U. Hübner, and D. Griebsch. *IEEE Transactions on Ultrasonics, Ferroelectrics and Frequency Control*, 49(3):383–392, 2002.

[20] R. Schröder. In *Proceedings 5th European Frequency and Time Forum*, pages 194–200, 1991.

[21] J. Vanier and C. Audoin. *The Quantum Physics of Atomic Frequency Standards*. Adam Hilger, Bristol and Philadelphia, 1989.

[22] S. Weyers, A. Bauch, U. Hübner, R. Schröder, and Chr. Tamm. *IEEE Transactions on Ultrasonics, Ferroelectrics and Frequency Control*, 47(2):432–437, 2000.

[23] S. Weyers, A. Bauch, D. Griebsch, U. Hübner, R. Schröder, and C. Tamm. In *Proceedings of the IEEE International Frequency Control Symposium and the 13th European Frequency and Time Forum*, pages 16–19, 1999.

[24] J. P. Barrat and C. Cohen-Tannoudji. *Journal de Physique et le Radium*, 22(6):329–336, 1961.
[25] W. Itano, L. L. Lewis, and D. Wineland. *Physical Review A*, 25(2):1235, 1982.
[26] P. Rosenbusch, S. Zhang, and A. Clairon. In *Proceedings of the IEEE International Frequency Control Symposium and the 21st European Frequency and Time Forum*, pages 1060–1063, 2007.
[27] E. J. Angstmann, V. A. Dzuba, and V. V. Flambaum. *Physical Review A*, 74:023405, 2006.
[28] B. Riedel. private communication.
[29] E. Tiesinga, B. J. Verhaar, H. T. C. Stoof, and D. van Bragt. *Physical Review A*, 45(5):R2671–R2673, 1992.
[30] S. R. Jefferts, J. Shirley, T. E. Parker, T. P. Heavner, D. M. Meekhof, C. Nelson, F. Levi, G. Constanzo, A. De Marchi, R. Drullinger, L. Hollberg, W. D. Lee, and F. L. Walls. *Metrologia*, 39:321–336, 2002.
[31] S. Ghezali, P. Laurent, S. N. Lea, and A. Clairon. *Europhysics Letters*, 36(1):25–30, 1996.
[32] K. Pöschl. *Mathematische Methoden der Hochfrequenztechnik*. Springer, Berlin, Göttingen, Heidelberg, 1956.
[33] E. Majorana. *Nuovo Cimento*, 9:4350, 1932.
[34] R. Wynands, R. Schröder, and S. Weyers. *IEEE Transactions on Instrumentation and Measurement*, 56(2):660–663, 2007.
[35] A. Bauch and R. Schröder. *Annalen der Physik*, 2:421–449, 1993.
[36] L. S. Cutler, C. A. Flory, R. P. Giffard, and A. De Marchi. *Journal of Applied Physics*, 69(5):2780–2792, 1991.
[37] C. Audoin, M. Jardino, L. S. Cutler, and R. F. Lacey. *IEEE Transactions on Instrumentation and Measurement*, 27(4):325–329, 1978.
[38] J. H. Shirley, T. P. Heavner, and S. R. Jefferts. *IEEE Transactions on Instrumentation and Measurement*, 58(4):1241–1246, 2009.
[39] A. Sen Gupta, R. Schröder, S. Weyers, and R. Wynands. In *Proceedings of the IEEE International Frequency Control Symposium and the 21st European Frequency and Time Forum*, pages 234–237, 2007.
[40] S. Weyers, R. Schröder, and R. Wynands. In *Proceedings of the 20th European Frequency and Time Forum*, pages 173–180, 2006.
[41] J. H. Shirley, F. Levi, T. P. Heavner, D. Calonico, D-H. Yu, and S. Jefferts. *IEEE Transactions on Ultrasonics, Ferroelectrics and Frequency Control*, 53(12):2376–2385, 2006.
[42] G. Santarelli, G. Governatori, D. Chambon, M. Lours, P. Rosenbusch, J. Guéna, F. Chapelet, S. Bize, M. E. Tobar, P. Laurent, T. Potier, and A. Clairon. *IEEE Transactions on Ultrasonics, Ferroelectrics and Frequency Control*, 56(7):1319–1326, 2009.
[43] S. Weyers, R. Wynands, K. Szymaniec, and W. Chalupczak. In *Proceedings of the IEEE International Frequency Control Symposium and the 21st European Frequency and Time Forum*, page 265, 2007.
[44] K. Szymaniec, W. Chalupczak, S. Weyers, and R. Wynands. *IEEE Transactions on Ultrasonics, Ferroelectrics and Frequency Control*, 54(9):1721–1722, 2006.
[45] K. Gibble. private communication.
[46] G. J. Dick. In *Proceedings of the 19th Annual Precise Time and Time Interval (PTTI) Applications and Planning Meeting*, page 133, 1987.
[47] G. Santarelli, P. Laurent, P. Lemonde, A. Clairon, A. G. Mann, S. Chang, A. N. Luiten, and C. Salomon. *Physical Review Letters*, 82:4619, 1999.
[48] BIPM CircularT, monthly, available at: http://www.bipm.org/jsp/en/TimeFtp.jsp.

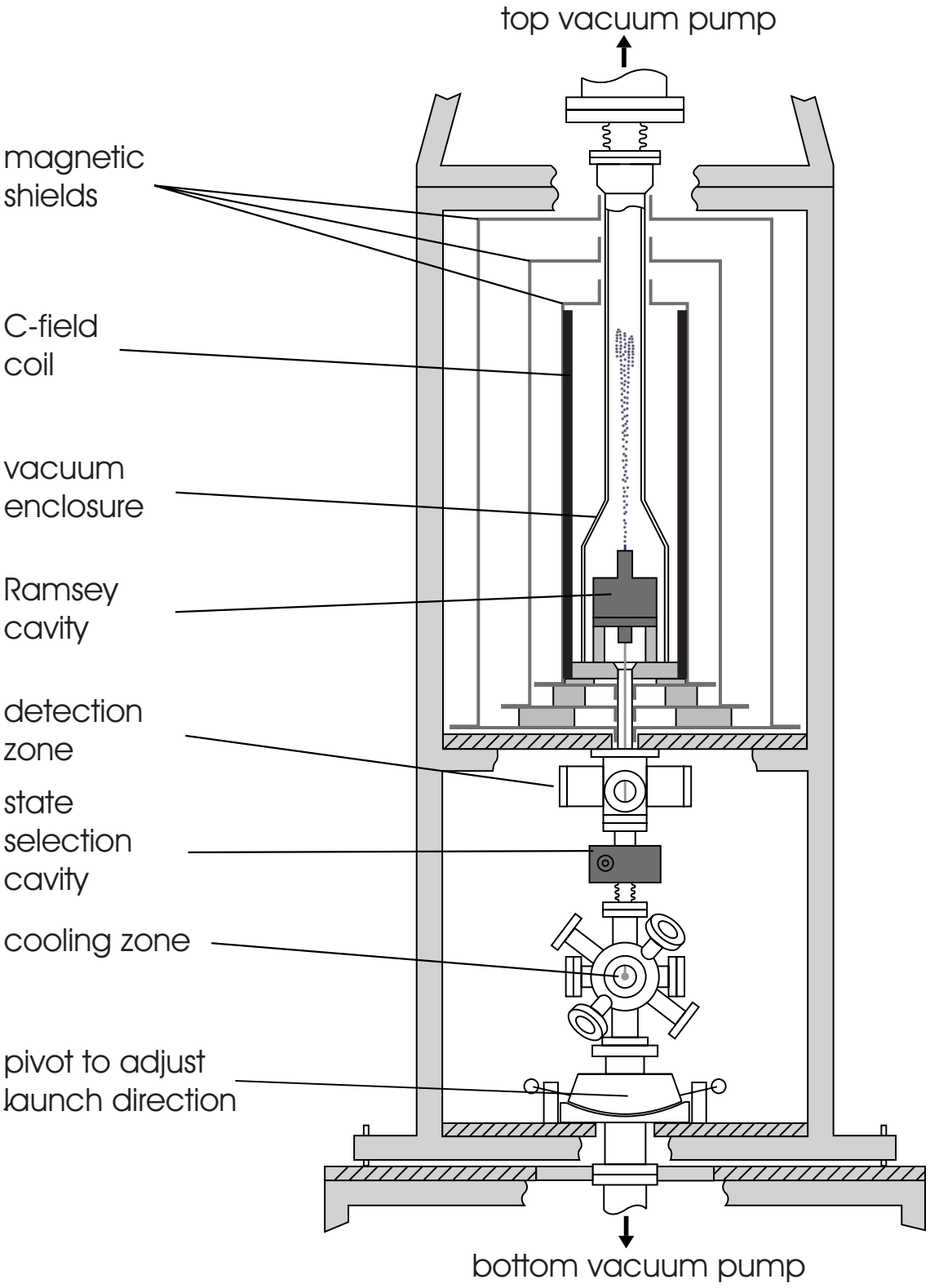

Figure 1. A schematic diagram of the CSF2 vacuum subsystem.

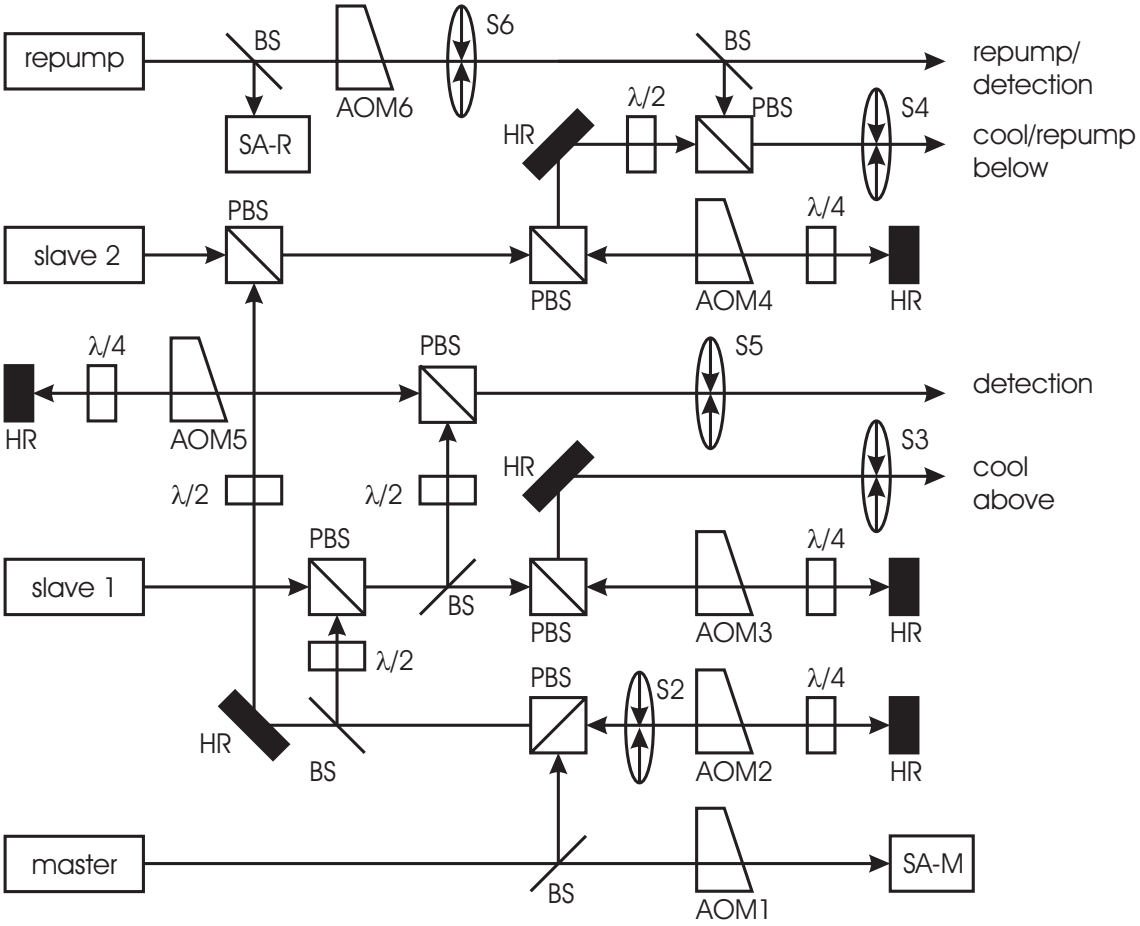

Figure 2. A simplified schematic of the optical system setup. AOM - acousto-optic modulator, S_i - shutter i, PBS - polarizing beam splitter, BS - beam splitter, HR - highly reflective mirror, $\lambda/2$ - halfwave plate, $\lambda/4$ - quarterwave plate, SA-M(R) – saturated-absorption spectroscopy master (repumping) laser.

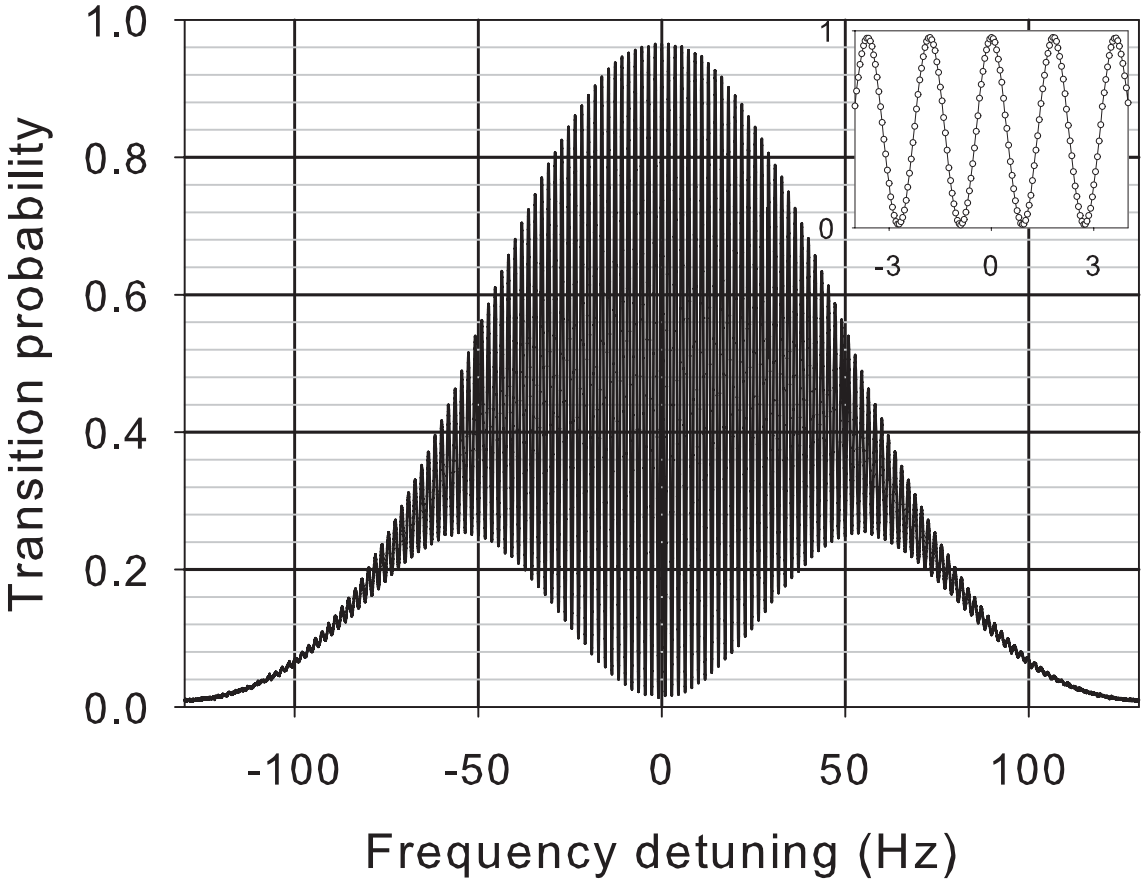

Figure 3. Ramsey fringe (one toss per point). The central fringe has a contrast of 95% and a width of 0.9 Hz.

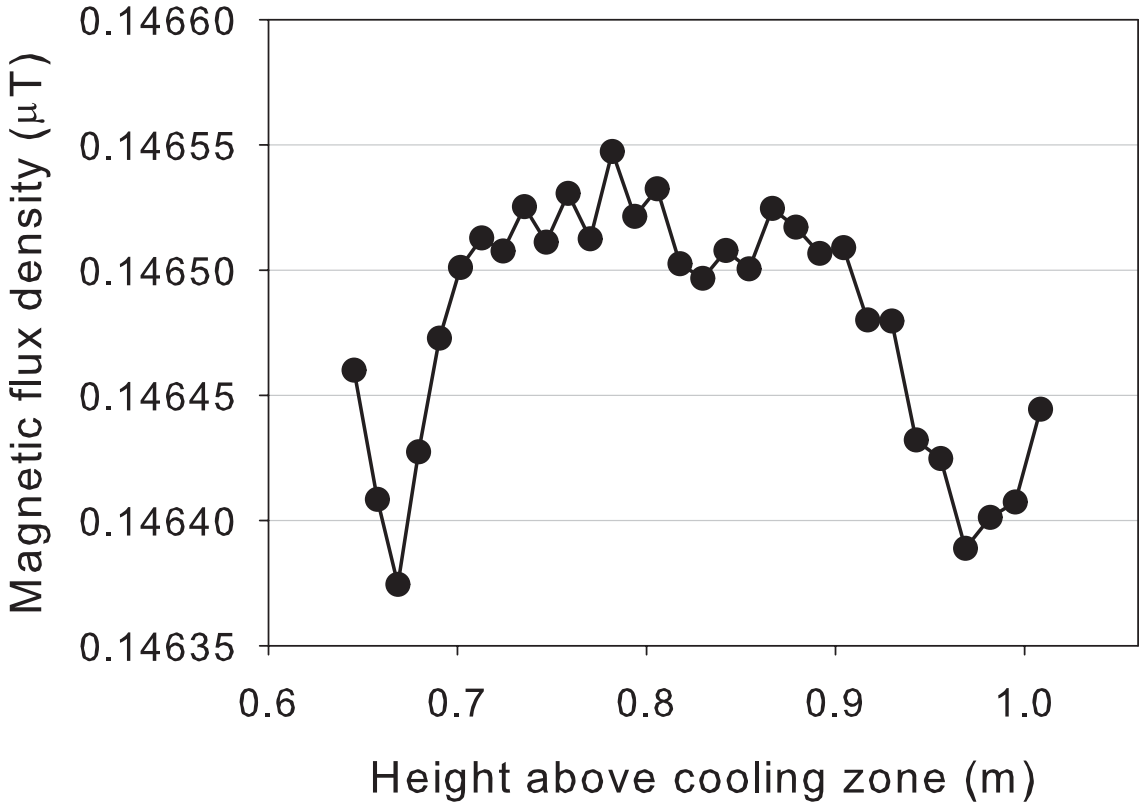

Figure 4. Magnetic field profile above the Ramsey cavity.

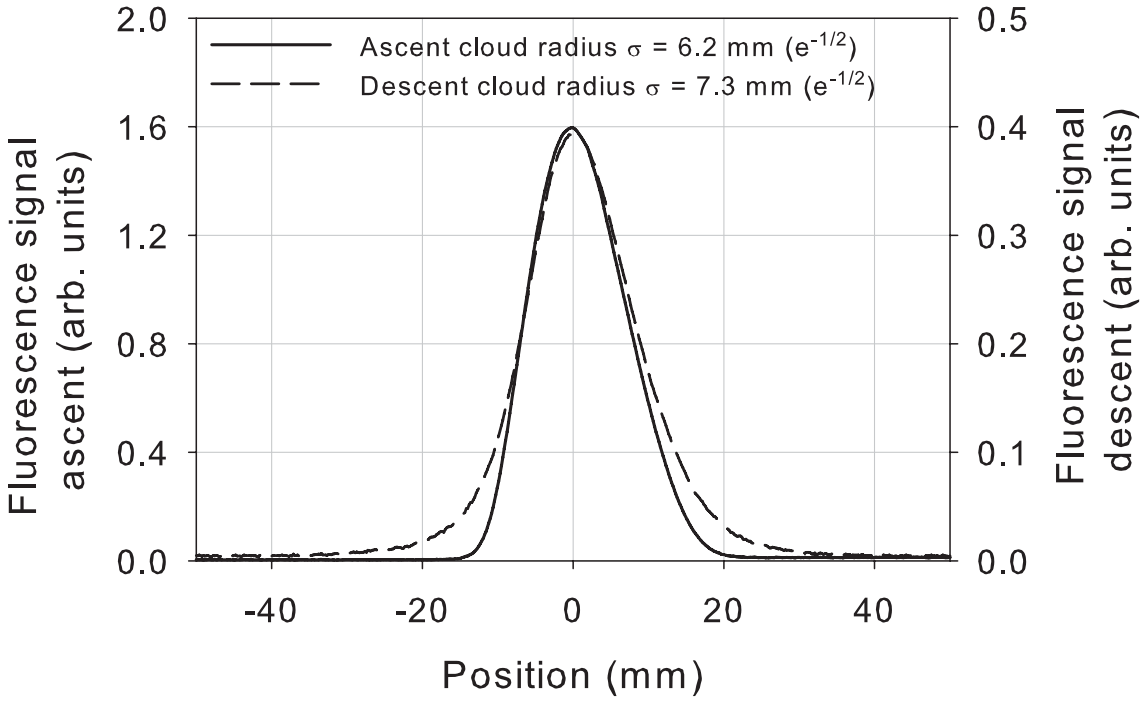

Figure 5. Atom number distribution in the atomic cloud, measured by monitoring the temporal change in fluorescence intensity as the atoms pass through the lower detection zone. Solid line - ascent, dashed line - descent.

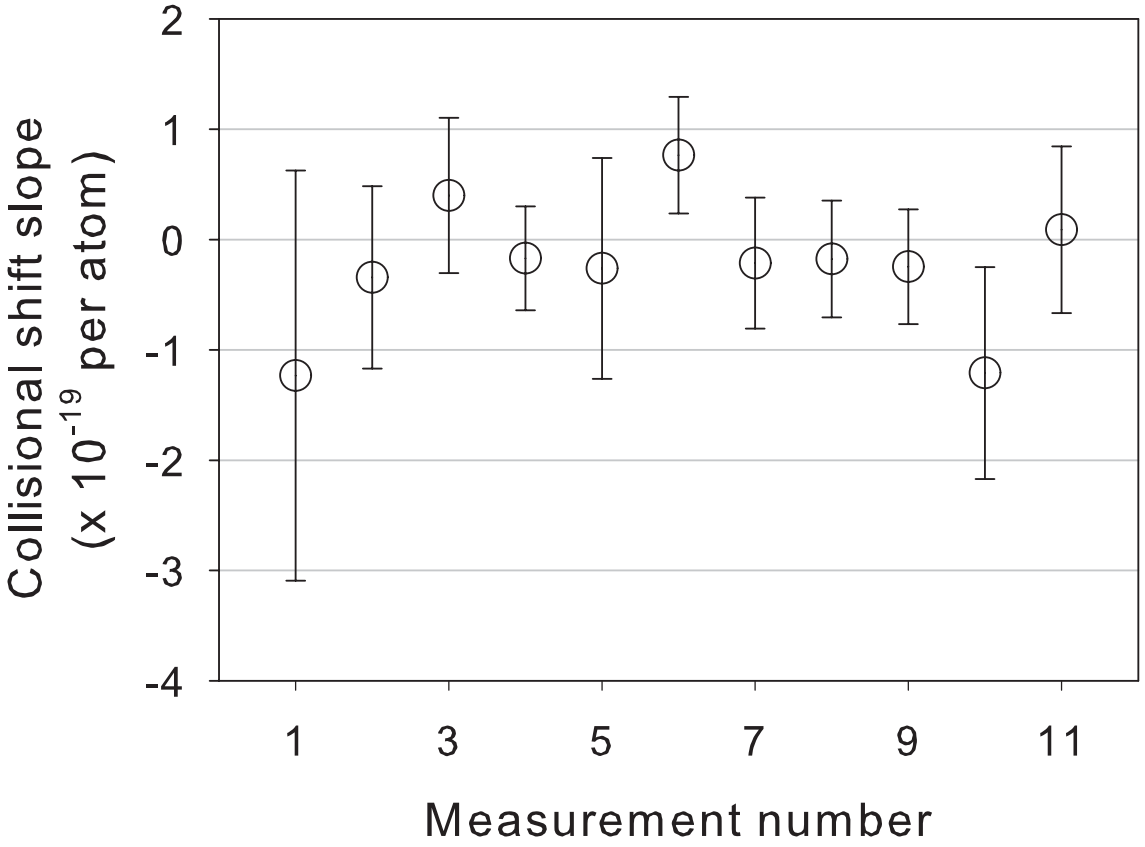

Figure 6. Measurements of the collisional shift slope (change of collisional shift as a function of the detected atom number in the state $|F = 4\rangle$).

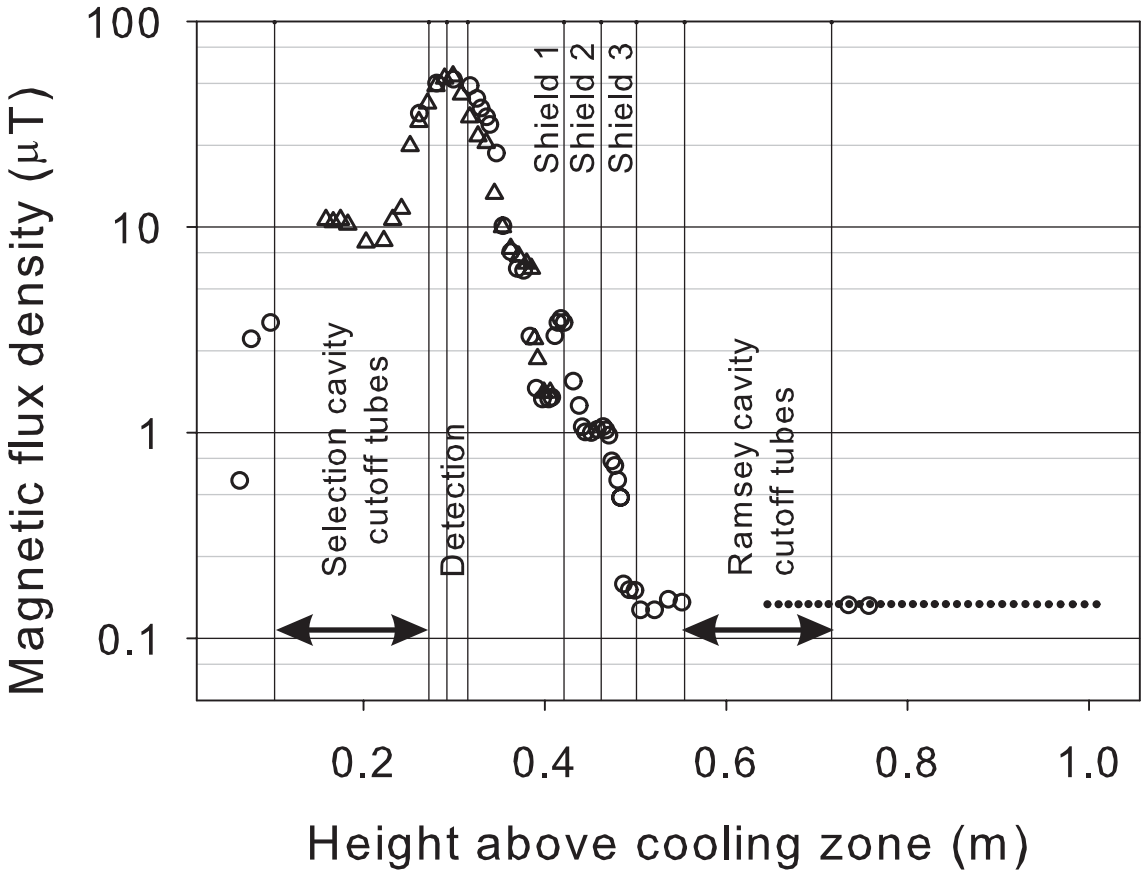

Figure 7. Modulus of the magnetic flux density as a function of height above the cooling zone, measured using three different methods to span the whole height range. Triangles - Zeeman transitions; open circles - hyperfine transitions; dots - using Ramsey cavity.

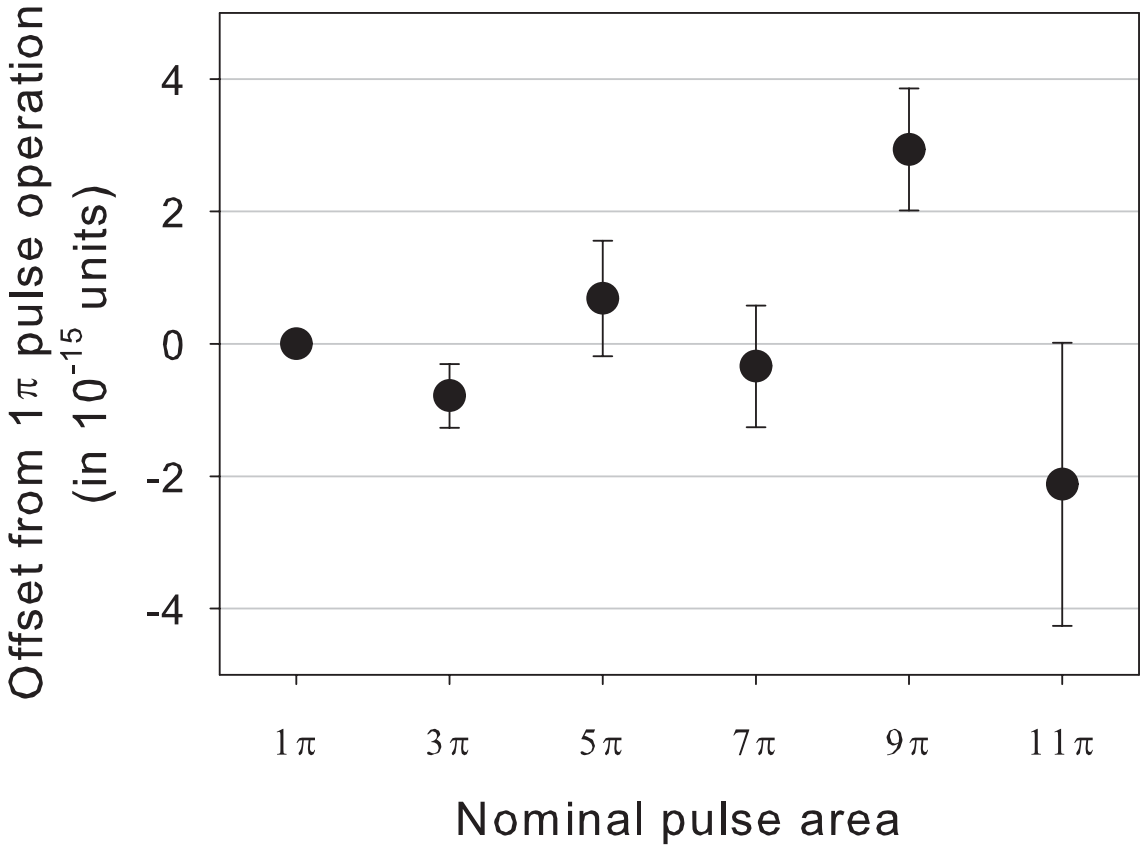

Figure 8. Microwave power-dependent frequency shifts for different microwave pulse areas $n\pi$. For each n, the state composition was adjusted to be the same as for $n = 1$. The shifts are given with respect to the fountain frequency at 1π pulse area operation.

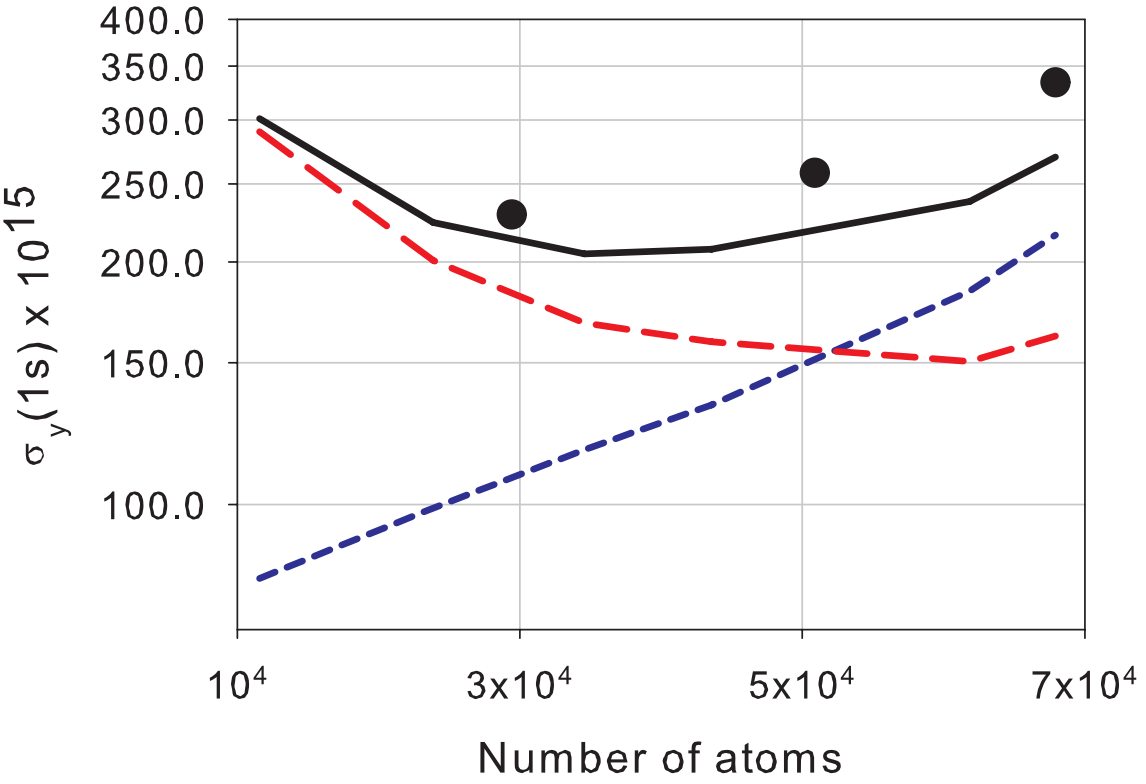

Figure 9. Allan deviation $\sigma_y\,(1\mathrm{s})$ for different detected atom numbers. Long-dashed line - contribution from the quantum projection noise (QPN); dashed line - contribution from the Dick effect; solid line - combined contribution of quantum projection noise and Dick effect; circles - measured Allan deviation with respect to PTB maser H6.

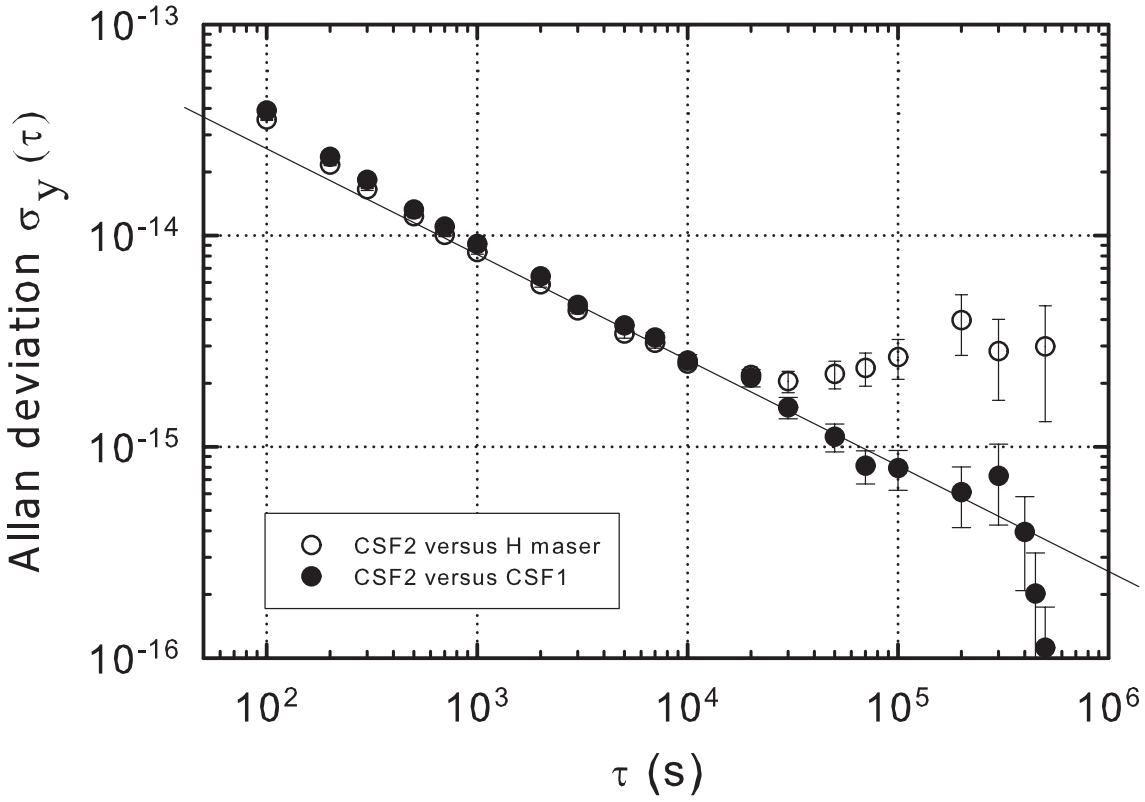

Figure 10. Allan standard deviation $\sigma_y(\tau)$ of CSF2 measured against hydrogen maser H6 (open circles) and CSF1 (solid circles) during 20 days.

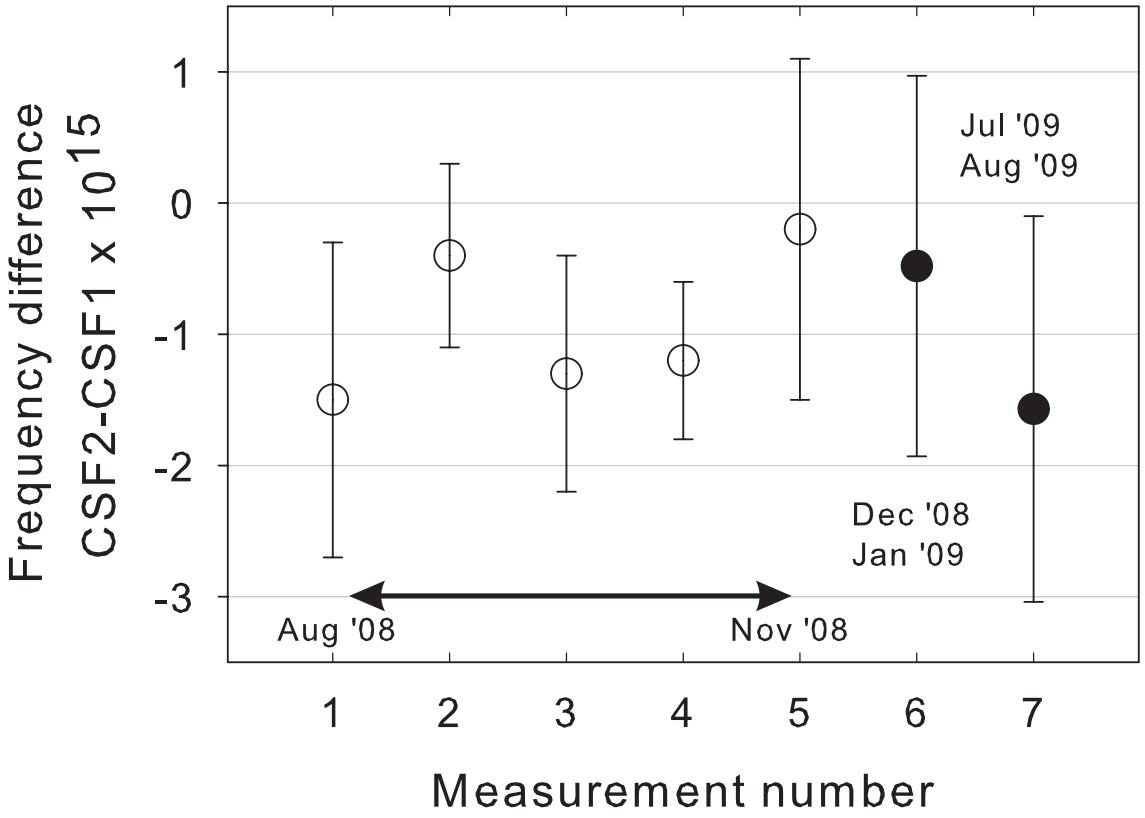

Figure 11. Fractional frequency difference between CSF2 and CSF1. Open circles represent measurements where the uncertainties of some systematic effects were not yet evaluated. Error bars indicate statistical uncertainties only. Solid circles - measurements with full systematic uncertainty evaluation. Error bars include statistical and systematic uncertainties.

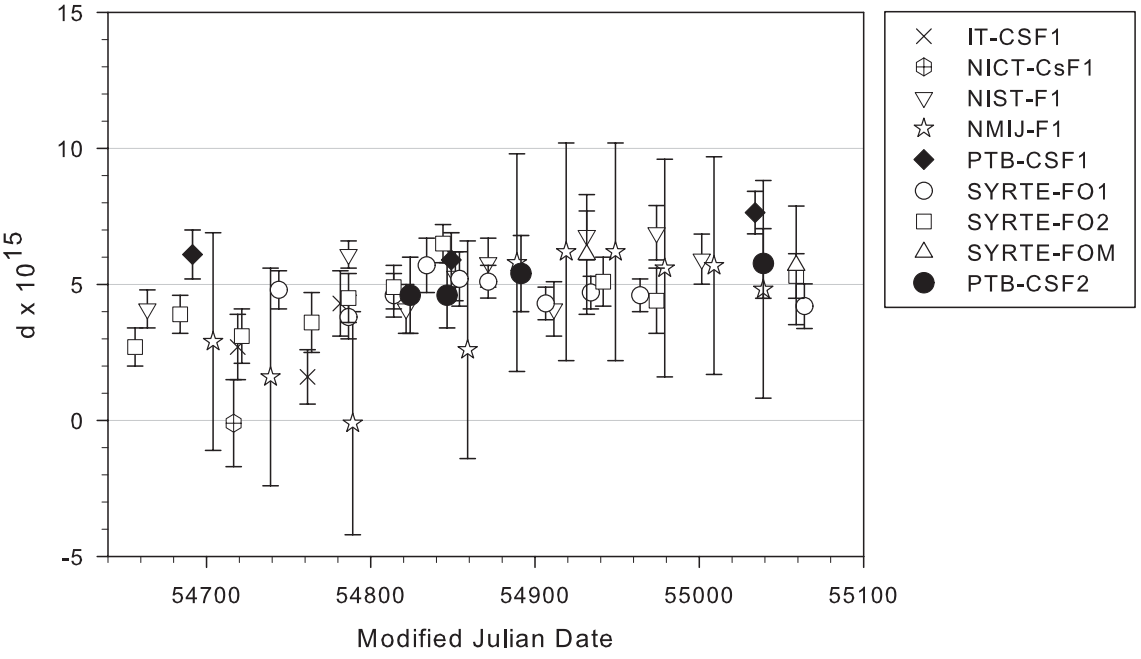

Figure 12. Fractional frequency offset d between primary fountain frequency standards and TAI.